SEARCH FOR PRODUCTION OF A HIGGS BOSON AND A SINGLE TOP QUARK IN MULTILEPTON FINAL STATES IN pp COLLISIONS AT $\sqrt{s} = 13$ TeV.

by

Jose Andres Monroy Montañez

A DISSERTATION

Presented to the Faculty of

The Graduate College at the University of Nebraska

In Partial Fulfilment of Requirements

For the Degree of Doctor of Philosophy

Major: Physics and Astronomy

Under the Supervision of Kenneth Bloom and Aaron Dominguez

Lincoln, Nebraska

July, 2018

SEARCH FOR PRODUCTION OF A HIGGS BOSON AND A SINGLE TOP QUARK IN MULTILEPTON FINAL STATES IN pp COLLISIONS AT $\sqrt{s} = 13$ TeV.

Jose Andres Monroy Montañez, Ph.D.

University of Nebraska, 2018

Adviser: Kenneth Bloom and Aaron Dominguez

Table of Contents

List of Figures

List of Tables

Chapter 1

INTRODUCTION

Figure 1.1: ^{14}N neutron capture in a PECVD polymerized pyridine film. The Q-value of this reaction is 626 keV. Taken from [22]

Chapter 2

Theoretical approach

2.1 Introduction

The physical description of the universe is a challenge that physicists have faced by making theories that refine existing principles and proposing new ones in an attempt to embrace emerging facts and phenomena.

At the end of 1940s Julian Schwinger [11] and Richard P. Feynman [12], based in the work of Sin-Itiro Tomonaga [13], developed an electromagnetic theory consistent with special relativity and quantum mechanics that describes how matter and light interact; the so-called "quantum eletrodynamics" (QED) had born.

QED has become the guide in the development of theories that describe the universe. It was the first example of a quantum field theory (QFT), which is the theoretical framework for building quantum mechanical models that describes particles and their interactions. QFT is composed of a set of mathematical tools that combines classical fields, special relativity and quantum mechanics, while keeping the quantum point particles and locality ideas.

This chapter gives an overview of the standard model of particle physics, starting with a description of the particles and interactions that compose it, followed by a description of the electroweak interaction, the Higgs boson and the associated production of Higgs boson and a single top quark (tH). The description contained in this chapter is based on references [1–3].

2.2 Standard model of particle physics

Particle physics at the fundamental level is modeled in terms of a collection of interacting particles and fields in a theory known as the "standard model of particle physics (SM)"[1].

The full picture of the SM is composed of three fields[2], whose excitations are interpreted as particles called mediators or force-carriers; a set of fields, whose excitations are interpreted as elementary particles, interacting through the exchange of those mediators and a field that gives the mass to elementary particles. Figure 2.1 shows an scheme of the SM particles organization. In addition to the particles in the scheme (but not listed in it), their corresponding anti-particles, with opposite quantum numbers, are also part of the picture; some particles are their own anti-particles, like photon or Higgs, or anti-particle is already listed like in the W^+ and W^- case.

The mathematical formulation of the SM is based on group theory and the use of

[1] The formal and complete treatment of the SM is out of the scope of this document, however a plenty of textbooks describing it at several levels are available in the literature. The treatment in "An Introduction To Quantum Field Theory (Frontiers in Physics)" by Michael E. Peskin and Dan V. Schroeder is quite comprehensive and detailed.

[2] Note that gravitational field is not included in the standard model formulation

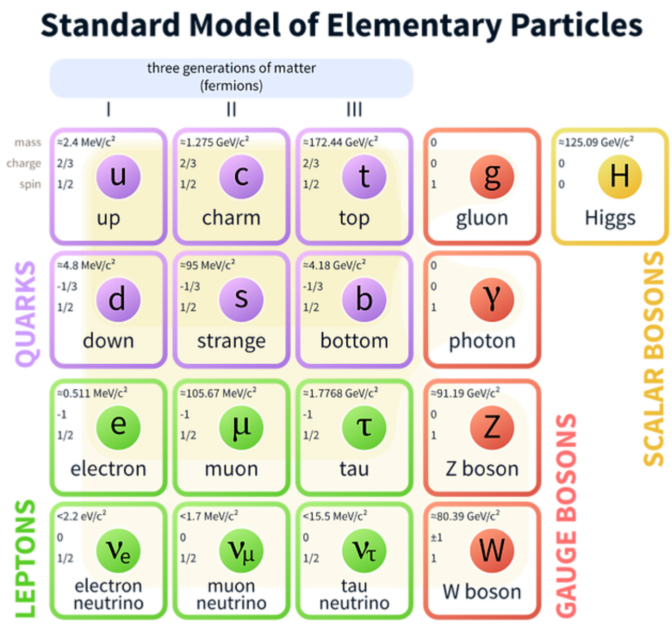

Figure 2.1: Schematic representation of the Standard model of particle physics. SM is a theoretical model intended to describe three of the four fundamental forces of the universe in terms of a set of particles and their interactions. [18].

Noether's theorem [17] which states that for a physical system modeled by a Lagrangian that is invariant under a group of transformations a conservation law is expected. For instance, a system described by a time-independent Lagrangian is invariant (symmetric) under time changes (transformations) with the total energy conservation law as the expected conservation law. In QED, the charge operator (Q) is the generator of the U(1) symmetry which according to the Noether's theorem means that there is a conserved quantity; this conserved quantity is the electric charge and thus the law conservation of electric charge is established.

In the SM, the symmetry group $SU(3)_C \otimes SU(2)_L \otimes U(1)_Y$ describes three of the four fundamental interactions in nature(see section 2.2.2): strong interaction(SI), weak interaction(WI) and electromagnetic interactions (EI) in terms of symmetries associated to physical quantities:

- Strong: $SU(3)_C$ associated to color charge
- Weak: $SU(2)_L$ associated to weak isospin and chirality
- Electromagnetic: $U(1)_Y$ associated to weak hypercharge and electric charge

It will be shown that the electromagnetic and weak interactions are combined in the so-called electroweak interaction where chirality, hypercharge, weak isospin and electric charge are the central concepts.

2.2.1 Fermions

The basic constituents of the ordinary matter at the lowest level, which form the set of elementary particles in the SM formulation, are quarks and leptons. All of them have spin 1/2, therefore they are classified as fermions since they obey Fermi-Dirac statistics. There are six "flavors" of quarks and three of leptons organized in three generations, or families, as shown in table 2.1.

		Generation		
	Type	1st	2nd	3rd
Leptons	Charged	Electron (e)	Moun(μ)	Tau (τ)
	Neutral	Electron neutrino (ν_e)	Muon neutrino (ν_μ)	Tau neutrino (ν_τ)
Quarks	Up-type	Up (u)	Charm (c)	Top (t)
	Down-type	Down (d)	Strange (s)	Bottom (b)

Table 2.1: Fermions of the SM. There are six flavors of quarks and three of leptons, organized in three generations, or families, composed of two pairs of closely related particles. The close relationship is motivated by the fact that WI between leptons is limited to the members of the same generation; WI between quarks is not limited but greatly favoured, to same generation members.

There is a mass hierarchy between generations (see table 2.2), where the higher generation particles decays to the lower one, which can explain why the ordinary matter is made of particles in the first generation. In the SM, neutrinos are modeled as massless particles so they are not subject to this mass hierarchy; however, today it is known that neutrinos are massive so the hierarchy could be restated. The reason behind this mass hierachy is one of the most important open questions in particle physics, and it becomes more puzzling when noticing that the mass difference between first and second generation fermions is small compared to the mass difference with respect to the third generation.

Lepton	Mass (MeV/c^2)	Quark	Mass (MeV/c^2)
e	0.51	u	2.2
μ	105.65	c	1.28×10^3
τ	1776.86	t	173.1×10^3
ν_e	Unknown	d	4.7
ν_μ	Unknown	s	96
τ_μ	Unknown	b	4.18×10^3

Table 2.2: Fermion masses [21]. Generations differ by mass in a way that have been interpreted as a masss hierarchy. Approximate values with no uncertainties are used, for comparison purpose.

Usually, the second and third generation fermions are produced in high energy processes, like the ones recreated in particle accelerators.

2.2.1.1 Leptons

A lepton is an elementary particle that is not subject to the SI. As seen in table 2.1, there are two types of leptons, the charged ones (electron, muon and tau) and the neutral ones (the three neutrinos). The electric charge (Q) is the property that gives leptons the ability to participate in the EI. From the classical point of view, Q plays a central role determining, among others, the strength of the electric field through which the electromagnetic force is exerted. It is clear that neutrinos are not affected by EI because they don't carry electric charge.

Another feature of the leptons that is fundamental in the mathematical description of the SM is the chirality, which is closely related to spin and helicity. Helicity defines the handedness of a particle by relating its spin and momentum such that if they are parallel then the particle is right-handed; if spin and momentum are antiparallel the particle is said to be left-handed. The study of parity conservation (or violation) in β-decay has shown that only left-handed electrons/neutrinos or right-handed positrons/anti-neutrinos are created [19]; the inclusion of that feature in the theory was achieved by using projection operators for helicity, however, helicity is frame dependent for massive particles which makes it not Lorentz invariant and then another related attribute has to be used: *chirality*.

Chirality is a purely quantum attribute which makes it not so easy to describe in graphical terms but it defines how the wave function of a particle transforms under certain rotations. As with helicity, there are two chiral states, left-handed chiral (L) and right-handed chiral (R). In the highly relativistic limit where $E \approx p \gg m$ helicity and chirality converge, becoming exactly the same for massless particles.

In the following, when referring to left-handed (right-handed) it will mean left-handed chiral (right-handed chiral). The fundamental fact about chirality is that while EI and SI are not sensitive to chirality, in WI left-handed and right-handed fermions are treated asymmetrically, such that only left handed fermions and right-handed anti-fermions are allowed to couple to WI mediators, which is a violation of parity. The way to translate this statement in a formal mathematical formulation is based on the isospin symmetry group $SU(2)_L$.

Each generation of leptons is seen as a weak isospin doublet.[3] The left-handed charged lepton and its associated left-handed neutrino are arranged in doublets of weak isospin T=1/2 while their right-handed partners are singlets:

$$\begin{pmatrix} \nu_l \\ l \end{pmatrix}_L, l_R := \begin{pmatrix} \nu_e \\ e \end{pmatrix}_L, \begin{pmatrix} \nu_\mu \\ \mu \end{pmatrix}_L, \begin{pmatrix} \nu_\tau \\ \tau \end{pmatrix}_L, e_R, \mu_R, \tau_R, \nu_{eR}, \nu_{\mu R}, \nu_{\tau R} \tag{2.1}$$

The isospin third component refers to the eigenvalues of the weak isospin operator which for doublets is $T_3 = \pm 1/2$, while for singlets it is $T_3 = 0$. The physical meaning of this doublet-singlet arrangement falls in that the WI couples the two particles in the doublet by exchanging the interaction mediator while the singlet member is not involved in WI. The main properties of the leptons are summarized in table 2.3.

Altough all three flavor neutrinos have been observed, their masses remain unknown and only some estimations have been made [20]. The main reason is that the flavor eigenstates are not the same as the mass eigenstates which implies that when a neutrino is created its mass state is a linear combination of the three mass eigenstates and experiments can only probe the squared difference of the masses. The Pontecorvo-Maki-Nakagawa-Sakata (PMNS) mixing matrix encode the relationship between flavor and mass eigenstates.

[3] The weak isospin is an analogy of the isospin symmetry in strong interaction where neutron and proton are affected equally by strong force but differ in their charge.

Lepton	Q(e)	T_3	L_e	L_μ	L_τ	Lifetime (s)
Electron (e)	-1	-1/2	1	0	0	Stable
Electron neutrino(ν_e)	0	1/2	1	0	0	Unknown
Muon (μ)	-1	-1/2	0	1	0	2.19×10^{-6}
Muon neutrino (ν_μ)	0	1/2	0	1	0	Unknown
Tau (τ)	-1	-1/2	0	0	1	290.3×10^{-15}
Tau neutrino (τ_μ)	0	1/2	0	0	1	Unknown

Table 2.3: Leptons properties [21]. Q: electric charge, T_3: weak isospin. Only left-handed leptons and right-handed anti-leptons participate in the WI. Anti-particles with inverted T_3, Q and lepton number complete the leptons set but are not listed. Right-handed leptons and left-handed anti-leptons, neither listed, form weak isospin singlets with $T_3 = 0$ and do not take part in the weak interaction.

2.2.1.2 Quarks

Quarks are the basic constituents of protons and neutrons. The way quarks join to form bound states, called "hadrons", is through the SI. Quarks are affected by all the fundamental interactions which means that they carry all the four types of charges: color, electric charge, weak isospin and mass.

Flavor	Q(e)	I_3	T_3	B	C	S	T	B'	Y	Color
Up (u)	2/3	1/2	1/2	1/3	0	0	0	0	1/3	r,b,g
Charm (c)	2/3	0	1/2	1/3	1	0	0	0	4/3	r,b,g
Top(t)	2/3	0	1/2	1/3	0	0	1	0	4/3	r,b,g
Down(d)	-1/3	-1/2	-1/2	1/3	0	0	0	0	1/3	r,b,g
Strange(s)	-1/3	0	-1/2	1/3	0	-1	0	0	-2/3	r,b,g
Bottom(b)	-1/3	0	-1/2	1/3	0	0	0	-1	-2/3	r,b,g

Table 2.4: Quarks properties [21]. Q: electric charge, I_3: isospin, T_3: weak isospin, B: baryon number, C: charmness, S: strangeness, T: topness, B': bottomness, Y: hypercharge. Anti-quarks posses the same mass and spin as quarks but all charges (color, flavor numbers) have opposite sign.

Table 2.4 summarizes the features of quarks, among which the most particular is their fractional electric charge. Note that fractional charge is not a problem, given that quarks are not found isolated, but serves to explain how composed particles are formed out of two or more valence quarks[4].

Color charge is the responsible for the SI between quarks and is the symmetry ($SU(3)_C$) that defines the formalism to describe SI. There are three colors: red (r), blue(b) and green(g) and their corresponding three anti-colors; thus each quark carries one color unit while anti-quarks carries one anti-color unit. As said above, quarks are not allowed to be isolated due to the color confinement effect, therefore their features have been studied indirectly by observing their bound states created when:

- one quark with a color charge is attracted by an anti-quark with the corresponding anti-color charge forming a colorless particle called a "meson."
- three quarks (anti-quarks) with different color (anti-color) charges are attracted among them forming a colorless particle called a "baryon(anti-baryon)."

In the first version of the quark model (1964), M. Gell-Mann [22] and G. Zweig [23, 24] developed a consistent way to classify hadrons according to their properties. Only three quarks (u, d, s) were involved in a scheme in which all baryons have baryon number B=1 and therefore quarks have B=1/3; non-baryons have B=0. The scheme organizes baryons in a two-dimensional space (I_3 - Y); Y (hypercharge) and I_3 (isospin) are quantum numbers related by the Gell-Mann-Nishijima formula [25, 26]:

$$Q = I_3 + \frac{Y}{2} \tag{2.2}$$

where $Y = B + S + C + T + B'$ are the quantum numbers listed in table 2.4. Baryon number is conserved in SI and EI which means that single quarks cannot be created

[4] Hadrons can contain an indefinite number of virtual quarks and gluons, known as the quark and gluon sea, but only the valence quarks determine hadrons' quantum numbers.

but in pairs $q - \bar{q}$.

There are six quark flavors organized in three generations (see table 2.1) following a mass hierarchy which, again, implies that higher generations decay to first generation quarks.

	Quarks			T_3	Y_W	Leptons			T_3	Y_W
Doublets	$\binom{u}{d'}_L$	$\binom{c}{s'}_L$	$\binom{t}{b'}_L$	$\binom{1/2}{-1/2}$	1/3	$\binom{\nu_e}{e}_L$	$\binom{\nu_\mu}{\mu}_L$	$\binom{\nu_\tau}{\tau}_L$	$\binom{1/2}{-1/2}$	-1
Singlets	u_R	c_R	t_R	0	4/3	ν_{eR}	$\nu_{\mu R}$	$\nu_{\tau R}$		
	d'_R	s'_R	b'_R	0	-2/3	e_R	μ_R	τ_R	0	-2

Table 2.5: Fermion weak isospin and weak hypercharge multiplets. Weak hypercharge is calculated through the Gell-Mann-Nishijima formula 2.2 but using the weak isospin and charge for quarks.

Isospin doublets of quarks are also defined (see table 2.5) and as for neutrinos, the mass eigenstates are not the same as the WI eigenstates which means that members of different quark generations are connected by the WI mediator; thus, up-type quarks are coupled not to down-type quarks directly but to a superposition of down-type quarks (q'_d) via WI according to:

$$
\begin{gathered}
q'_d = V_{CKM}\, q_d \\
\begin{pmatrix} d' \\ s' \\ b' \end{pmatrix} = \begin{pmatrix} V_{ud} & V_{us} & V_{ub} \\ V_{cd} & V_{cs} & V_{cb} \\ V_{td} & V_{ts} & V_{tb} \end{pmatrix} \begin{pmatrix} d \\ s \\ b \end{pmatrix}
\end{gathered}
\tag{2.3}
$$

where V_{CKM} is known as Cabibbo-Kobayashi-Maskawa (CKM) mixing matrix [27,28]. The weak decays of quarks are represented in the diagram of figure 2.2; again the CKM matrix plays a central role since it contains the probabilities for the different

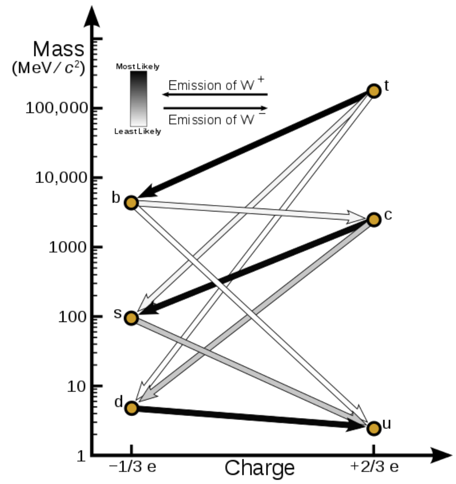

Figure 2.2: Transformations between quarks through WI. Higher generations quarks decay to first generation quarks by emitting a W boson. The arrow color indicates the likelihood of the transition according to the grey scale in the top left side which represent the CKM matrix parameters [29].

quark decay channels, in particular, note that quark decays are greatly favored between generation members.

CKM matrix is a 3×3 unitary matrix parametrized by three mixing angles and the *CP-mixing phase*; the latter is the parameter responsible for the Charge-Parity symmetry violation (CP-violation) in the SM. The fact that the b quark decays almost all the times to a top quark is exploided in this thesis when making the selection of the signal events by requiring the presence of a jet tagged as a jet comming from a b quark in the final state. The effect of the *CP-mixing phase* on the cross section of associated production of Higss boson and a single top process is also explored in this thesis.

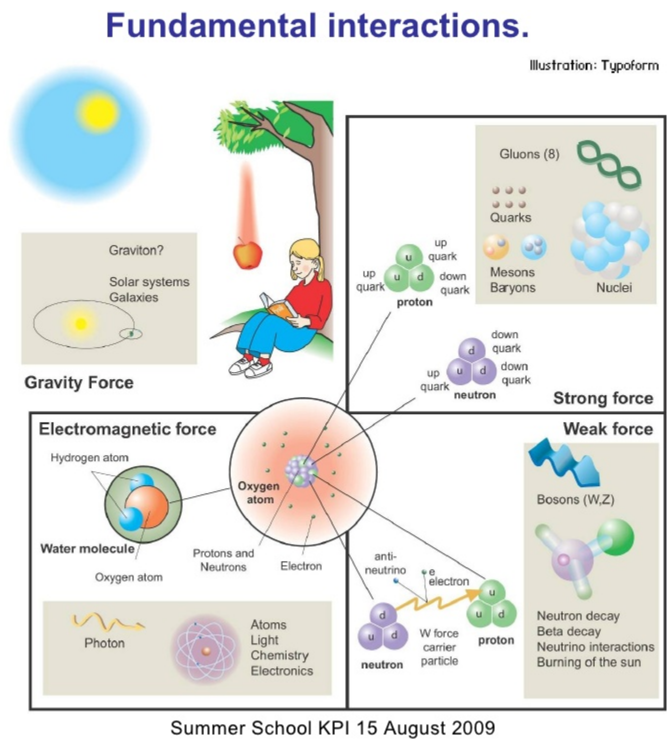

Figure 2.3: Fundamental interactions in nature. Despite the many manifestations of forces in nature, we can track all of them back to one of the fundamental interactions. The most common forces are gravity and electromagnetic given that all of us are subject and experience them in everyday life.

2.2.2 Fundamental interactions

Even though there are many manifestations of force in nature, like the ones represented in figure 2.3, we can classify all of them into one of four fundamental interactions:

- *Electromagnetic interaction (EI)* affects particles that are "electrically charged," like electrons and protons. It is described by QED combining quantum mechanics, special relativity and electromagnetism in order to explain how particles with electric charge interact through the exchange of photons, therefore, one says that "Electomagnetic Force" is mediated by "photons". Figure 2.4a. shows a graphical representation, known as "feynman diagram", of electron-electron scattering.

- *Strong interaction (SI)* described by Quantum Chromodynamics (QCD). Hadrons like proton and neutron have internal structure given that they are composed of two or more valence quarks[5]. Quarks have fractional electric charge which means that they are subject to electromagnetic interaction and in the case of the proton they should break appart due to electrostatic repulsion; however, quarks are held together inside the hadrons against their electrostatic repulsion by the "Strong Force" through the exchange of "gluons." The analog to the electric charge is the "color charge". Electrons and photons are elementary particles as quarks but they don't carry color charge, therefore they are not subject to SI. The feynman diagram for gluon exchange between quarks is shown in figure 2.4b.

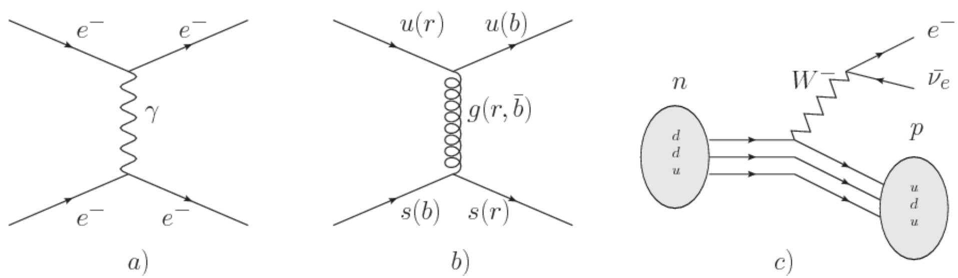

Figure 2.4: Feynman diagrams representing the interactions in SM; a) EI: e-e scattering; b) SI: gluon exchange between quarks ; c) WI: β-decay

- *Weak interaction (WI)* described by the weak theory (WT), is responsible, for instance, for the radioactive decay in atoms and proton-proton (pp) fusion within the sun. Quarks and leptons are the particles affected by the weak interaction; they possess a property called "flavor charge" (see 2.2.1) which can be changed by emitting or absorbing one weak force mediator. There are three mediators of the "weak force" known as "Z" boson in the case of electrically

[5] particles made of four and five quarks are exotic states not so common.

neutral changes and "$W^{\pm}$" bosons in the case of electrically charged changes. The "weak isospin" is the WI analog to electric charge in EI, and color charge in SI, and defines how quarks and leptons are affected by the weak force. Figure 2.4c. shows the feynman diagram of β-decay where a newtron (n) is transformed in a proton (p) by emmiting a W^- particle. Since this thesis is in the frame of the electroweak interaction, a more detailed description of it will be given in section 2.3

- *Gravitational interaction (GI)* described by General Theory of Relativity (GR). It is responsible for the structure of galaxies and black holes as well as the expansion of the universe. As a classical theory, in the sense that it can be formulated without even appeal to the concept of quantization, it implies that the spacetime is a continuum and predictions can be made without limitation to the precision of the measurement tools. The latter represent a direct contradiction of the quantum mechanics principles. Gravity is deterministic while quantum mechanics is probabilistic; despite that, efforts to develop a quantum theory of gravity have predicted the "graviton" as mediator of the Gravitational force[6].

Interaction	Acts on	Relative strength	Range (m)	Mediators
Electromagnetic (QED)	Electrically charged particles	10^{-2}	Infinite	Photon
Strong (QCD)	Quarks and gluons	1	10^{-15}	Gluon
Weak (WI)	Leptons and quarks	10^{-6}	10^{-18}	$W^{\pm}$, Z
Gravitational (GI)	Massive particles	10^{-39}	Infinite	Graviton

Table 2.6: Fundamental interactions features [30].

Table 2.6 sumarizes the main features of the fundamental interactions. The relative strength of the fundamental forces reveals the meaning of strong and weak; in

[6] Actually a wide variety of theories have been developed in an attempt to describe gravity; some famous examples are string theory and supergravity.

a context where the relative strength of the SI is 1, the EI is about hundred times weaker and WI is about million times weaker thant the SI. A good description on how the relative strenght and range of the fundamental intreractions are calculated can be found in references [30, 31]. In the everyday life, only EI and GI are explicitly experienced due to the range of these interactions; i.e., at the human scale distances only EI and GI have appreciable effects, in contrast to SI which at distances greater than 10^{-15}m become negligible.

QED was built successfully on the basis of the classical electrodynamics theory (CED) of Maxwell and Lorentz, following theoretical and experimental requirements imposed by

- lorentz invariance: independence on the reference frame.
- locallity: interacting fields are evaluated at the same space-time point to avoid action at a distance.
- renormalizability: physical predictions are finite and well defined
- particle spectrum, symmetries and conservation laws already known must emerge from the theory.
- gauge invariance.

The gauge invariance requirement reflects the fact that the fundamental fields cannot be directly measured but associated fields which are the observables. Electric (**"E"**) and magnetic (**"B"**) fields in CED are associated with the electric scalar potential "V" and the vector potential **"A"**. In particular, **E** can be obtained by measuring the change in the space of the scalar potential (ΔV); however, two scalar potentials differing by a constant “f” correspond to the same electric field. The same happens in the case of the vector potential **“A”**; thus, different configurations of the associated fields result in the same set of values of the observables. The freedom in choosing one particular configuration is known as “gauge freedom”; the tranformation law connecting two configurations is known as “gauge transformation” and the fact that the observables are not affected by a gauge transformation is called “gauge invariance”.

When the gauge tranformation:

$$\begin{aligned} \mathbf{A} \rightarrow & \mathbf{A} - \Delta f \\ V \rightarrow & V - \frac{\partial f}{\partial t} \end{aligned} \tag{2.4}$$

is applied to Maxwell equations, they are still satisfied and the fields remain invariant. Thus, CED is invariant under gauge transformations and is called a “gauge theory”. The set of all gauge transformations form the “symmetry group” of the theory, which according to the group theory, has a set of “group generators”. The number of group generators determine the number of “gauge fields” of the theory.

As mentioned in the first lines of section 2.2, QED has one symmetry group (U(1)) with one group generator (the Q operator) and one gauge field (the electromagnetic field A^{μ}). In CED there is not a clear definition, beyond the historical convention, of which fields are the fundamental and which are the associated, but in QED it is clear that the fundamental field is A^{μ}. When a gauge theory is quantized, the gauge field is quantized and its quanta is called “gauge boson”. The word boson characterizes particles with integer spin which obvey Bose-einstein statistics.

As will be detailed in section 2.3, interactions between partcles in a system can be obtained by considering first the Lagrangian density of free particles in the system, which of course is incomplete because the interaction terms have been left out, and demanding global phase transformation invariance. Global phase transformation invariance means that a gauge transformation is performed identically to every point in the space[7] and the Lagrangian remains invariant. Then, the global transformation is promoted to a local phase transformation (this time the gauge transformation depends on the position in space) and again invariance is required.

Due to the space dependence of the local tranformation, the Lagrangian density is not invariant anymore. In order to restate the gauge invariance, the gauge covariant derivative is introduced in the Lagrangian and with it the gauge field responsible for the interaction between particles in the system. The new Lagrangian density is gauge invariant, includes the interaction terms needed to account for the interactions and provides a way to explain the interaction between particles through the exchange of the gauge boson.
This recipe was used to build QED and the theories that aim to explain the fundamental interactions.

2.2.3 Gauge Bosons

The importance of the gauge bosons comes from the fact that they are the force mediators or force carriers. The features of the gauge bosons reflect those of the fields they represent and they are extracted from the Lagrangian density used to describe the interactions. In section 2.3, it will be shown how the gauge bosons of the

[7] Here space corresponds to the 4-dimensional space i.e. space-time.

EI and WI emerge from the electroweak Lagrangian. The SI gauge bosons features are also extracted from the SI Lagrangian but it is not detailed in this document. The main features of the SM gauge bosons will be briefly presented below and summarized in table 2.7.

- **Photon**. EI occurs when the photon couples to (is exchanged between) particles carrying electric charge; however, the photon itself does not carry electric charge, therefore, there is no coupling between photons. Given that the photon is massless the EI is of infinite range, i.e., electrically charged particles interact even if they are located far away one from each other; this also implies that photons always move with the speed of light.

- **Gluon**. SI is mediated by gluons which, same as photons, are massless. They carry one unit of color charge and one unit of anticolor charge which means that gluons couple to other gluons. As a result, the range of the SI is not infinite but very short due to the attraction between gluons, giving rise to the "color confinement" which explains why color charged particles cannot be isolated but live within composited particles, like quarks inside protons.

- **W, Z**. The WI mediators, $W^{\pm}$ and Z, are massive which explains their short-range. Given that the WI is the only interaction that can change the flavor of the interacting particles, the W boson is the responsible for the nuclear transmutation where a neutron is converted in a proton or vice versa with the involvement of an electron and a neutrino (see figure 2.4c). The Z boson is the responsible of the neutral weak processes like neutrino elastic scattering where no electric charge but momentum transference is involved. WI gauge bosons carry isospin charge which makes posible the interaction between them.

Interaction	Mediator	Electric charge (e)	Color charge	Weak Isospin	mass (GeV/c^2)
Electromagnetic	Photon (γ)	0	No	0	0
Strong	Gluon (g)	0	Yes -octet	No	0
Weak	$W^{\pm}$	± 1	No	± 1	80.385 $\pm$ 0.015
	Z	0	No	0	91.188 $\pm$ 0.002

Table 2.7: SM gauge bosons main features [21].

2.3 Electroweak unification and the Higgs mechanism

Physicists dream of building a theory that contains all the interactions in one single interaction, i.e., showing that at some scale in energy all the four fundamental interactions are unified and only one interaction emerges in a "Theory of everything". The first sign of the feasibility of such unification comes from success in the construction of the CED. Einstein spent years trying to reach that dream, which by 1920 only involved electromagnetism and gravity, with no success; however, a new partial unification was achieved in the 1960's, when S.Glashow [14], A.Salam [15] and S.Weinberg [16] independently proposed that electromagnetic and weak interactions are two manifestations of a more general interaction called "electroweak interaction (EWT)". Both, QCD and EWT, were developed in parallel and following the useful prescription provided by QED and the gauge invariance principles.

The theory of weak interactions was capable of explaining the β-decay and in general the processes mediated by $W^{\pm}$ bosons. However, there were some processes like the "$\nu_\mu - e$ scattering" which would require the exchange of two W bosons (see figure 2.5 top diagrams) giving rise to divergent loop integrals and then non finite predictions.

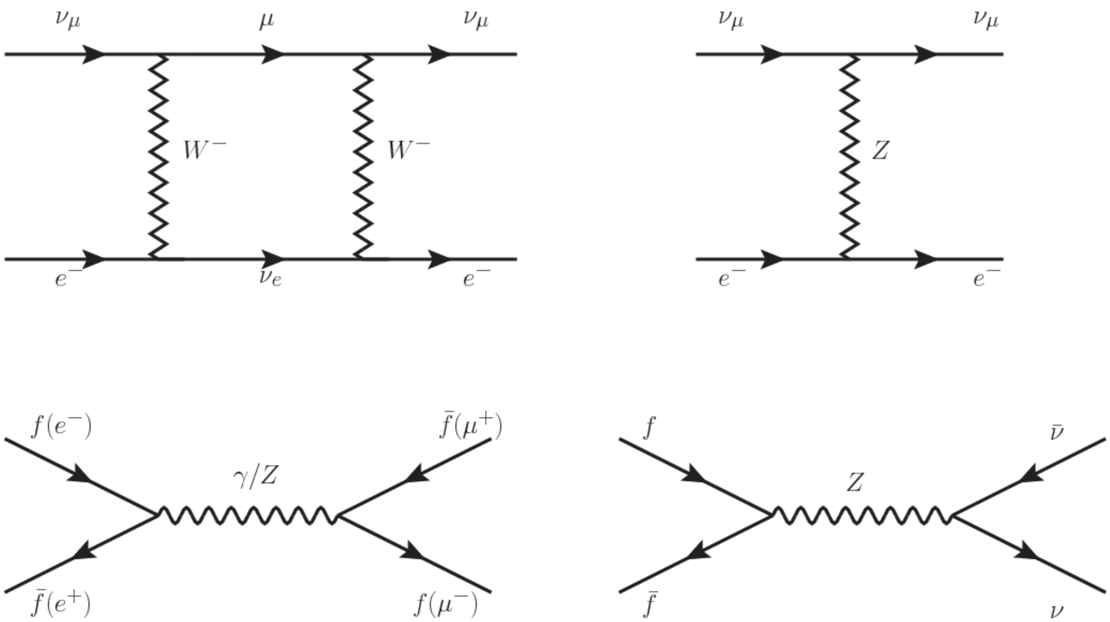

Figure 2.5: Top: $\nu_\mu - e^-$ scattering going through charged currents (left) and neutral currents (right). Bottom: neutral current processes for charged fermions (left) and involving neutrinos (right). While neutral current processes involving only charged fermions can proceed through EI or WI, those involving neutrinos can only proceed via WI.

By including neutral currents involving fermions via the exchange of neutral bosons Z, those divergences are compensated and the predictions become realistic.

Neutral weak interaction vertices conserve flavor in the same way as the electromagnetic vertices do, but additionally, the Z boson can couple to neutrinos which implies that processes involving charged fermions can proceed through EI or WI but processes involving neutrinos can proceed only through WI.

The prescription to build a gauge theory of the WI consists of proposing a free field Lagrangian density that includes the particles involved; next, by requesting invariance under global phase transformations first and generalizing to local phase transformations invariance later, the conserved currents are identified and interactions are generated by introducing gauge fields. Given that the goal is to include the EI and WI in a single theory, the group symmetry considered should be a combination of $SU(2)_L$ and $U(1)_{em}$, however the latter cannot be used directly because the EI treats left and right-handed particles indistinctly in contrast to the former. Fortunately, the weak hypercharge, which is a combination of the weak isospin and the electric charge (eqn 2.2) is suitable to be used since it is conserved by the EI and WI. Thus, the symmetry group to be considered is

$$G \equiv SU(2)_L \otimes U(1)_Y \tag{2.5}$$

The following treatment applies to any of the fermion generations, but for simplicity the first generation of leptons will be considered [2, 3, 32, 33].

Given the first generation of leptons

$$\psi_1 = \begin{pmatrix} \nu_e \\ e^- \end{pmatrix}_L, \qquad \psi_2 = \nu_{eR}, \qquad \psi_3 = e^-_R \tag{2.6}$$

the charged fermionic currents are given by

$$J_\mu \equiv J^+_\mu = \bar{\nu}_{eL}\gamma_\mu e_L, \qquad J^\dagger_\mu \equiv J^-_\mu = \bar{e}_L\gamma_\mu\nu_{eL} \tag{2.7}$$

and the free Lagrangian is given by

$$\mathcal{L}_0 = \sum_{j=1}^{3} i\overline{\psi}_j(x)\gamma^\mu\partial_\mu\psi_j(x). \tag{2.8}$$

Mass terms are included directly in the QED and QCD free Lagrangians since they preserve the invariance under the symmetry transformations involved which treat left-handed and right-handed similarly, however mass terms of the form

$$m_W^2 W_\mu^\dagger(x) W^\mu(x) + \frac{1}{2} m_Z^2 Z_\mu(x) Z^\mu(x) - m_e \bar{\psi_e}(x) \psi_e(x) \tag{2.9}$$

which represent the mass of $W^\pm$, Z and electrons, are not invariant under G transformations, therefore the gauge fields described by the EWI are in principle massless.

Experiments have shown that the gauge fields are not massless; however, they have to acquire mass through a mechanism compatible with the gauge invariance; that mechanism is known as the "Higgs mechanism" and will be considered later in this section. The global transformations in the combined symmetry group G can be written as

$$\begin{aligned} \psi_1(x) &\xrightarrow{G} \psi_1'(x) \equiv U_Y U_L \psi_1(x), \\ \psi_2(x) &\xrightarrow{G} \psi_2'(x) \equiv U_Y \psi_2(x), \\ \psi_3(x) &\xrightarrow{G} \psi_3'(x) \equiv U_Y \psi_3(x) \end{aligned} \tag{2.10}$$

where U_L represent the $SU(2)_L$ transformation acting only on the weak isospin doublet and U_Y represent the $U(1)_Y$ transformation acting on all the weak isospin multiplets. Explicitly

$$U_L \equiv \exp\left(i\frac{\sigma_i}{2}\alpha^i\right), \qquad U_Y \equiv \exp(iy_i\beta) \qquad (i = 1,2,3) \tag{2.11}$$

with σ_i the Pauli matrices and y_i the weak hypercharges. In order to promote the transformations from global to local while keeping the invariance, it is required that $\alpha^i = \alpha^i(x)$, $\beta = \beta(x)$ and the replacement of the ordinary derivatives by the covariant derivatives

$$
\begin{aligned}
D_\mu\psi_1(x) &\equiv \left[\partial_\mu + ig\sigma_i W^i_\mu(x)/2 + ig' y_1 B_\mu(x)\right]\psi_1(x) \\
D_\mu\psi_2(x) &\equiv \left[\partial_\mu + ig' y_2 B_\mu(x)\right]\psi_2(x) \\
D_\mu\psi_3(x) &\equiv \left[\partial_\mu + ig' y_3 B_\mu(x)\right]\psi_3(x)
\end{aligned}
\tag{2.12}
$$

introducing in this way four gauge fields, $W^i_\mu(x)$ and $B_\mu(x)$, in the process. The covariant derivatives (eqn 2.12) are required to transform in the same way as fermion fields $\psi_i(x)$ themselves, therefore, the gauge fields transform as:

$$
\begin{aligned}
B_\mu(x) \xrightarrow{G} B'_\mu(x) \equiv& B_\mu(x) - \frac{1}{g'}\partial_\mu\beta(x) \\
W^i_\mu(x) \xrightarrow{G} W^{i\prime}_\mu(x) \equiv& W^i_\mu(x) - \frac{i}{g}\partial_\mu\alpha_i(x) - \varepsilon_{ijk}\alpha_i(x)W^i_\mu(x).
\end{aligned}
\tag{2.13}
$$

The G invariant version of the Lagrangian density 2.8 can be written as

$$
\mathcal{L}_0 = \sum_{j=1}^{3} i\overline{\psi}_j(x)\gamma^\mu D_\mu\psi_j(x) \tag{2.14}
$$

where free massless fermion and gauge fields and fermion-gauge boson interactions are included. The EWI Lagrangian density must additionally include kinetic terms for the gauge fields ($\mathcal{L}_G$) which are built from the field strengths, according to

$$
B_{\mu\nu}(x) \equiv \partial_\mu B_\nu - \partial_\nu B_\mu \tag{2.15}
$$

$$
W^i_{\mu\nu}(x) \equiv \partial_\mu W^i_\nu(x) - \partial_\nu W^i_\mu(x) - g\varepsilon^{ijk}W^j_\mu W^k_\nu \tag{2.16}
$$

the last term in eqn. 2.16 is added in order to hold the gauge invariance; therefore,

$$\mathcal{L}_G = -\frac{1}{4}B_{\mu\nu}(x)B^{\mu\nu}(x) - \frac{1}{4}W^i_{\mu\nu}(x)W_i^{\mu\nu}(x) \tag{2.17}$$

which contains not only the free gauge fields contributions, but also the gauge fields self-interactions and interactions among them.

The three weak isospin conserved currents resulting from the $SU(2)_L$ symmetry are given by

$$J^i_\mu(x) = \frac{1}{2}\bar{\psi}_1(x)\gamma_\mu\sigma^i\psi_1(x) \tag{2.18}$$

while the weak hypercharge conserved current resulting from the $U(1)_Y$ symmetry is given by

$$J^Y_\mu = \sum_{j=1}^{3}\overline{\psi}_j(x)\gamma_\mu y_j\psi_j(x) \tag{2.19}$$

In order to evaluate the electroweak interactions modeled by an isotriplet field W^i_μ which couples to isospin currents J^i_μ with strength g and additionally the singlet field B_μ which couples to the weak hypercharge current J^Y_μ with strength $g'/2$. The interaction Lagrangian density to be considered is

$$\mathcal{L}_I = -gJ^{i\mu}(x)W^i_\mu(x) - \frac{g'}{2}J^{Y\mu}(x)B_\mu(x) \tag{2.20}$$

Note that the weak isospin currents are not the same as the charged fermionic currents that were used to describe the WI (eqn 2.7), since the weak isospin eigenstates are not the same as the mass eigenstates, but they are closely related

$$J_\mu = \frac{1}{2}(J^1_\mu + iJ^2_\mu), \qquad J^\dagger_\mu = \frac{1}{2}(J^1_\mu - iJ^2_\mu). \tag{2.21}$$

The same happens with the gauge fields W_μ^i which are related to the mass eigenstates $W^\pm$ by

$$W_\mu^+ = \frac{1}{\sqrt{2}}(W_\mu^1 - iW_\mu^2), \qquad W_\mu^- = \frac{1}{\sqrt{2}}(W_\mu^1 + iW_\mu^2). \tag{2.22}$$

The fact that there are three weak isospin conserved currents is an indication that in addition to the charged fermionic currents, which couple charged to neutral leptons, there should be a neutral fermionic current that does not involve electric charge exchange; therefore, it couples neutral fermions or fermions of the same electric charge. The third weak isospin current contains a term that is similar to the electromagnetic current (j_μ^{em}), indicating that there is a relation between them and resembling the Gell-Mann-Nishijima formula 2.2 adapted to electroweak interactions

$$Q = T_3 + \frac{Y_W}{2}. \tag{2.23}$$

Just as Q generates the $U(1)_{em}$ symmetry, the weak hypercharge generates the $U(1)_Y$ symmetry as said before. It is possible to write the relationship in terms of the currents as

$$j_\mu^{em} = J_\mu^3 + \frac{1}{2}J_\mu^Y. \tag{2.24}$$

The neutral gauge fields W_μ^3 and B_μ cannot be directly identified with the Z and the photon fields since the photon interacts similarly with left and right-handed fermions; however, they are related through a linear combination given by

$$\begin{aligned} A_\mu =& B_\mu \cos\theta_W + W_\mu^3 \sin\theta_W \\ Z_\mu =& -B_\mu \sin\theta_W + W_\mu^3 \cos\theta_W \end{aligned} \tag{2.25}$$

where θ_W is known as the "Weinberg angle." The interaction Lagrangian is now given by

$$\mathcal{L}_I = -\frac{g}{\sqrt{2}}(J^\mu W_\mu^+ + J^{\mu\dagger} W_\mu^-) - \left(g\sin\theta_W J_\mu^3 + g'\cos\theta_W \frac{J_\mu^Y}{2} \right) A^\mu - \left(g\cos\theta_W J_\mu^3 - g'\sin\theta_W \frac{J_\mu^Y}{2} \right) Z^\mu \tag{2.26}$$

the first term is the weak charged current interaction, while the second term is the electromagnetic interaction under the condition

$$g\sin\theta_W = g'\cos\theta_W = e, \quad \frac{g'}{g} = tan\theta_W \tag{2.27}$$

contained in the eqn.2.24; the third term is the neutral weak current.

Note that the neutral fields transformation given by the eqn. 2.25 can be written in terms of the coupling constants g and g' as:

$$A_\mu = \frac{g' W_\mu^3 + g B_\mu}{\sqrt{g^2 + g'^2}}, \qquad Z_\mu = \frac{g W_\mu^3 - g' B_\mu}{\sqrt{g^2 + g'^2}} \tag{2.28}$$

So far, the Lagrangian density describing the non-massive EWI is:

$$\mathcal{L}_{nmEWI} = \mathcal{L}_0 + \mathcal{L}_G \tag{2.29}$$

where fermion and gauge fields have been considered massless because their regular mass terms are manifestly non invariant under G transformations; therefore, masses have to be generated in a gauge invariant way. The mechanism by which this goal is achieved is known as the "Higss mechanism" and is closely connected to the concept of "spontaneous symmetry breaking."

2.3.1 Spontaneous symmetry breaking (SSB)

Figure 2.6 left shows a steel nail (top) which is subject to an external force; the form of the potential energy is also shown (bottom).

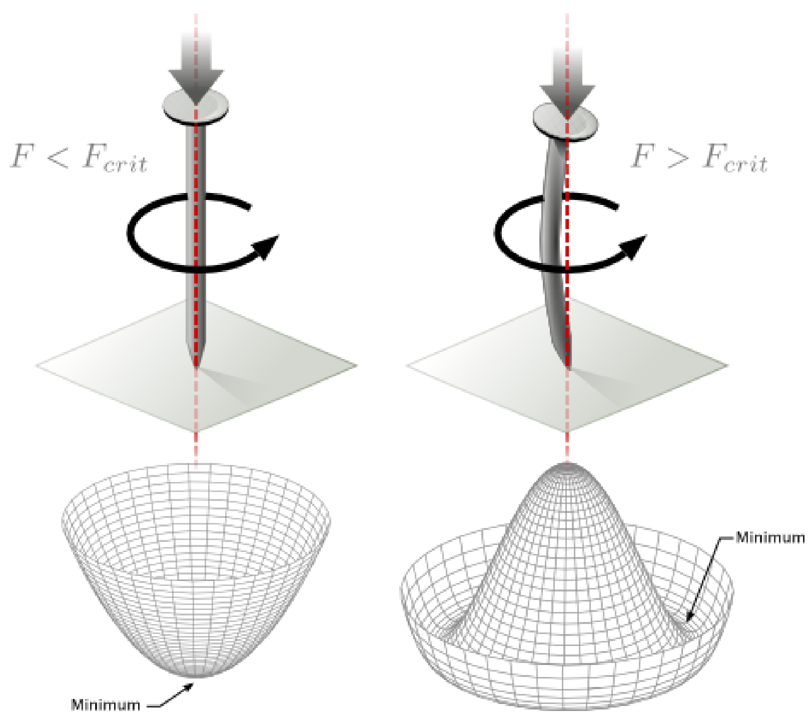

Figure 2.6: Spontaneous symmetry breaking mechanism. The steel nail, subject to an external force (top left), has rotational symmetry with respect to its axis. When the external force overcomes a critical value the nail buckles (top right) choosing a minimal energy state (ground state) and thus *"breaking spontoaneously the rotational symmetry"*. The potential energy (bottom) changes but holds the rotational symmetry; however, an infinite number of asymmetric ground states are generated and circularly distributed in the bottom of the potential [34].

Before reaching the critical force value, the system has rotational symmetry with respect to the nail axis; however, after the critical force value is reached the nail buckles (top right). The form of the potential energy (bottom right) changes, preserving its rotational symmetry although its minima does not exhibit that rotational symmetry any longer. Right before the nail buckles there is no indication of the direction the nail will bend because any of the directions are equivalent, but once the nail bends, choosing a direction, an arbitrary minimal energy state (ground state) is selected and it does not share the system's rotational symmetry. This mechanism for reaching an asymmetric ground state is known as *"spontaneous symmetry breaking"*.
The lesson from this analysis is that the way to introduce the SSB mechanism into a system is by adding the appropriate potential to it.

Figure 2.7 shows a plot of the potential $V(\phi)$ in the case of a scalar field ϕ

$$V(\phi) = \mu^2\phi^\dagger\phi + \lambda(\phi^\dagger\phi)^2 \tag{2.30}$$

If $\mu^2 > 0$ the potential has only one minimum at $\phi = 0$ and describes a scalar field with mass μ. If $\mu^2 < 0$ the potential has a local maximum at $\phi = 0$ and two minima at $\phi = \pm\sqrt{-\mu^2/\lambda}$ which enables the SSB mechanism to work.

In the case of a complex scalar field $\phi(x)$

$$\phi(x) = \frac{1}{\sqrt{2}}(\phi_1 + i\phi_2) \tag{2.31}$$

the Lagrangian (invariant under global $U(1)$ transformations) is given by

$$\mathcal{L} = (\partial_\mu\phi)^\dagger(\partial^\mu\phi) - V(\phi), \qquad V(\phi) = \mu^2\phi^\dagger\phi + \lambda(\phi^\dagger\phi)^2 \tag{2.32}$$

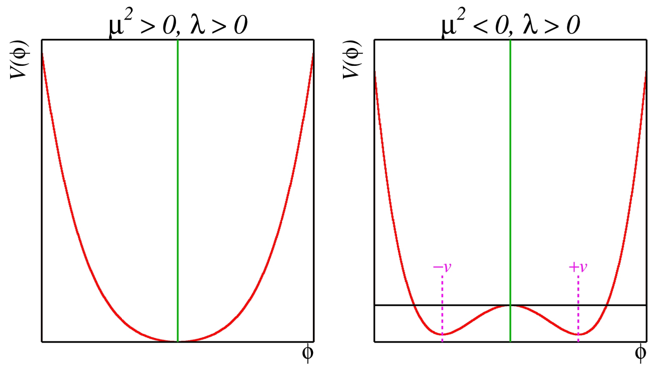

Figure 2.7: Shape of the potential $V(\phi)$ for $\lambda > 0$ and: $\mu^2 > 0$ (left) and $\mu^2 < 0$ (right). The case $\mu^2 < 0$ corresponds to the potential suitable for introducing the SSB mechanism by choosing one of the two ground states which are connected via refletion symmetry. [34].

where an appropiate potential has been added in order to introduce the SSB.

As seen in figure 2.8, the potential has now an infinite number of minima circularly distributed along the ξ-direction which makes possible the occurence of the SSB by choosing an arbitrary ground state; for instance, $\xi = 0$, i.e. $\phi_1 = v, \phi_2 = 0$

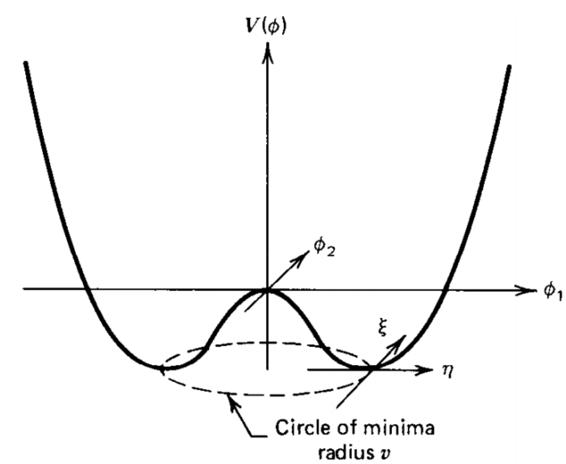

Figure 2.8: Potential for complex scalar field. There is a circle of minima of radius v along the ξ-direction [3].

$$\phi_0 = \frac{v}{\sqrt{2}} \exp(i\xi) \quad \xrightarrow{SSB} \quad \phi_0 = \frac{v}{\sqrt{2}} \tag{2.33}$$

As usual, excitations over the ground state are studied by making an expansion about it; thus, the excitation can be parametrized as:

$$\phi(x) = \frac{1}{\sqrt{2}}(v + \eta(x) + i\xi(x)) \tag{2.34}$$

which when substituted into eqn. 2.32 produces a Lagrangian in terms of the new fields η and ξ

$$\mathcal{L}' = \frac{1}{2}(\partial_\mu \xi)^2 + \frac{1}{2}(\partial_\mu \eta)^2 + \mu^2\eta^2 - V(\phi_0) - \lambda v \eta(\eta^2 + \xi^2) - \frac{\lambda}{4}(\eta^2 + \xi^2)^2 \tag{2.35}$$

where the last two terms represent the interactions and self-interaction between the two fields η and ξ. The particular feature of the SSB mechanism is revealed when looking to the first three terms of $\mathcal{L}'$. Before the SSB, only the massless ϕ field is present in the system; after the SSB there are two fields of which the η-field has acquired mass $m_\eta = \sqrt{-2\mu^2}$ while the $\xi - field$ is still massless (see figure 2.9).

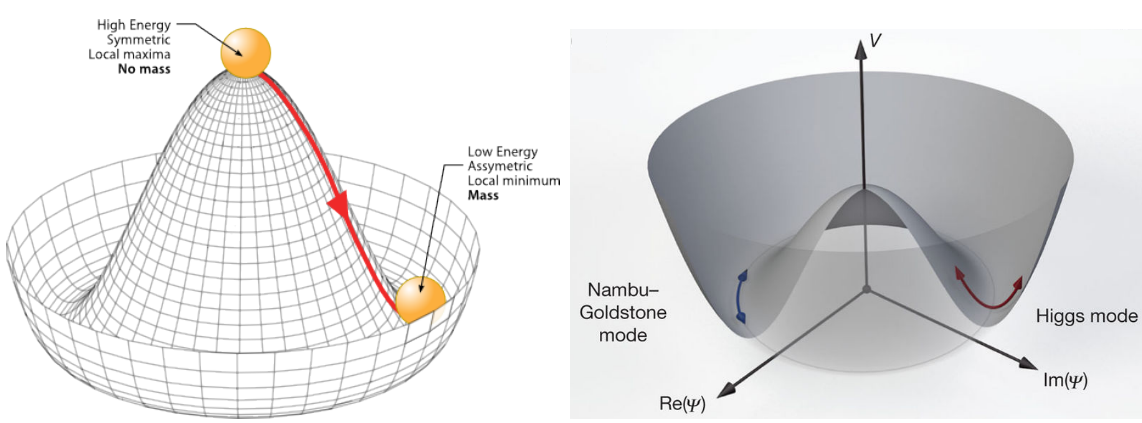

Figure 2.9: SSB mechanism for a complex scalar field [34, 35].

Thus, *the SSB mechanism serves as a method to generate mass but as a side effect a* *massless field is introduced in the system.* This fact is known as the Goldstone theorem and states that a massless scalar field appears in the system for each continuous symmetry spontaneously broken. Another version of the Goldstone theorem states that *"if a Lagrangian is invariant under a continuous symmetry group G, but the vacuum is only invariant under a subgroup $H \subset G$, then there must exist as many massless spin-0 particles (Nambu-Goldstone bosons) as broken generators."* [33] The Nambu-Goldstone boson can be understood considering that the potential in the ξ-direction is flat so excitations in that direction are not energy consuming and thus represent a massless state.

2.3.2 Higgs mechanism

When the SSB mechanism is introduced in the formulation of the EWI in an attempt to generate the mass of the so far massless gauge bosons and fermions, an interesting effect is revealed. In order to keep the G symmetry group invariance and generate the mass of the EW gauge bosons, a G invariant Lagrangian density ($\mathcal{L}_S$) has to be added to the non massive EWI Lagrangian (eqn. 2.29)

$$\mathcal{L}_S = (D_\mu \phi)^\dagger (D^\mu \phi) - \mu^2 \phi^\dagger \phi - \lambda (\phi^\dagger \phi)^2, \qquad \lambda > 0, \mu^2 < 0 \tag{2.36}$$

$$D_\mu \phi = \left(i\partial_\mu - g\frac{\sigma_i}{2} W_\mu^i - g' \frac{Y}{2} B_\mu \right) \phi \tag{2.37}$$

ϕ has to be an isospin doublet of complex scalar fields so it preserves the G invariance; thus ϕ can be defined as:

$$\phi = \begin{pmatrix} \phi^+ \\ \phi^0 \end{pmatrix} \equiv \frac{1}{\sqrt{2}} \begin{pmatrix} \phi_1 + i\phi_2 \\ \phi_3 + i\phi_4 \end{pmatrix}. \tag{2.38}$$

The minima of the potential are defined by

$$\phi^\dagger\phi = \frac{1}{2}(\phi_1^2+\phi_2^2+\phi_3^2+\phi_1^4) = -\frac{\mu^2}{2\lambda}. \tag{2.39}$$

The choice of the ground state is critical. By choosing a ground state, invariant under $U(1)_{em}$ gauge symmetry, the photon will remain massless and the $W^\pm$ and Z bosons masses will be generated which is exactly what is needed. In that sense, the best choice corresponds to a weak isospin doublet with $T_3 = -1/2$, $Y_W = 1$ and $Q = 0$ which defines a ground state with $\phi_1 = \phi_2 = \phi_4$ and $\phi_3 = v$:

$$\phi_0 \equiv \frac{1}{\sqrt{2}}\begin{pmatrix}0\\ v\end{pmatrix}, \qquad v^2 \equiv -\frac{\mu^2}{\lambda}. \tag{2.40}$$

where the vacuum expectation value v is fixed by the Fermi coupling G_F according to $v = (\sqrt{2}G_F)^{1/2} \approx 246$ GeV.

The G symmetry has been broken and three Nambu-Goldstone bosons will appear. The next step is to expand ϕ about the chosen ground state as:

$$\phi(x) = \frac{1}{\sqrt{2}}\exp\left(\frac{i}{v}\sigma_i\theta^i(x)\right)\begin{pmatrix}0\\ v+H(x)\end{pmatrix} \approx \frac{1}{\sqrt{2}}\begin{pmatrix}\theta_1(x)+i\theta_2(x)\\ v+H(x)-i\theta_3(x)\end{pmatrix} \tag{2.41}$$

to describe fluctuations from the ground state ϕ_0. The fields $\theta_i(x)$ represent the Nambu-Goldstone bosons while $H(x)$ is known as “higgs field.” The fundamental feature of the parametrization used is that the dependence on the $\theta_i(x)$ fields is factored out in a global phase that can be eliminated by taking the physical “unitary gauge” $\theta_i(x) = 0$. Therefore the expansion about the ground state is given by:

$$\phi(x)\frac{1}{\sqrt{2}}\begin{pmatrix}0\\ v+H(x)\end{pmatrix} \tag{2.42}$$

which when substituted into $\mathcal{L}_S$ (eqn. 2.36) results in a Lagrangian containing the now massive three gauge bosons $W^{\pm}, Z$, one massless gauge boson (photon) and the new Higgs field (H). The three degrees of freedom corresponding to the Nambu-Goldstone bosons are now integrated into the massive gauge bosons as their longitudinal polarizations which were not available when they were massless particles. The effect by which vector boson fields acquire mass after an spontaneous symmetry breaking, but without an explicit gauge invariance breaking is known as the *"Higgs mechanism"*.

The mechanism was proposed by three independent groups: F.Englert and R.Brout in August 1964 [36], P.Higgs in October 1964 [37] and G.Guralnik, C.Hagen and T.Kibble in November 1964 [38]; however, its importance was not realized until S.Glashow [14], A.Salam [15] and S.Weinberg [16], independently, proposed that electromagnetic and weak interactions are two manifestations of a more general interaction called "electroweak interaction" in 1967.

2.3.3 Masses of the gauge bosons

The mass of the gauge bosons is extracted by evaluating the kinetic part of Lagrangian $\mathcal{L}_S$ in the ground state (known also as the vacuum expectation value), i.e.,

$$\left|\left(\partial_\mu - ig\frac{\sigma_i}{2}W^i_\mu - i\frac{g'}{2}B_\mu\right)\phi_0\right|^2 = \left(\frac{1}{2}vg\right)^2 W^+_\mu W^{-\mu} + \frac{1}{8}v^2(W^3_\mu, B_\mu)\begin{pmatrix} g^2 & -gg' \\ -gg' & g'^2 \end{pmatrix}\begin{pmatrix} W^{3\mu} \\ B^\mu \end{pmatrix} \tag{2.43}$$

comparing with the typical mass term for a charged boson $M_W^2 W^+ W^-$

$$M_W = \frac{1}{2}vg. \tag{2.44}$$

The second term in the right side of the eqn.2.43 comprises the masses of the neutral bosons, but it needs to be written in terms of the gauge fields Z_μ and A_μ in order to be compared to the typical mass terms for neutral bosons, therefore using eqn. 2.28

$$\begin{aligned}\frac{1}{8}v^2[g^2(W_\mu^3)^2 - 2gg'W_\mu^3 B^\mu + g'^2 B_\mu^2] &= \frac{1}{8}v^2[gW_\mu^3 - g'B_\mu]^2 + 0[g'W_\mu^3 + gB_\mu]^2 \\ &= \frac{1}{8}v^2[\sqrt{g^2+g'^2}Z_\mu]^2 + 0[\sqrt{g^2+g'^2}A_\mu]^2\end{aligned} \tag{2.45}$$

and then

$$M_Z = \frac{1}{2}v\sqrt{g^2+g'^2}, \qquad M_A = 0 \tag{2.46}$$

2.3.4 Masses of the fermions

The lepton mass terms can be generated by introducing a gauge invariant Lagrangian term describing the Yukawa coupling between the lepton field and the Higgs field

$$\mathcal{L}_{Yl} = -G_l\left[(\bar{\nu}_l, \bar{l})_L \begin{pmatrix}\phi^+ \\ \phi^0\end{pmatrix} l_R + \bar{l}_R(\phi^-, \bar{\phi}^0)\begin{pmatrix}\nu_l \\ l\end{pmatrix}_L\right], \qquad l = e, \mu, \tau. \tag{2.47}$$

After the SSB and replacing the usual field expansion about the ground state (eqn.2.40) into $\mathcal{L}_{Yl}$, the mass term arises

$$\mathcal{L}_{Yl} = -m_l(\bar{l}_L l_R + \bar{l}_R l_L) - \frac{m_l}{v}(\bar{l}_L l_R + \bar{l}_R l_L)H = -m_l \bar{l}l\left(1 + \frac{H}{v}\right) \tag{2.48}$$

$$m_l = \frac{G_l}{\sqrt{2}}v \tag{2.49}$$

where the additional term represents the lepton-Higgs interaction. The quark masses are generated in a similar way as lepton masses but for the upper member of the quark doublet a different Higgs doublet is needed:

$$\phi_c = -i\sigma_2\phi* = \begin{pmatrix} -\bar{\phi}^0 \\ \phi^- \end{pmatrix}. \tag{2.50}$$

Additionally, given that the quark isospin doublets are not constructed in terms of the mass eigenstates but in terms of the flavor eigenstates, as shown in table2.5, the coupling parameters will be related to the CKM matrix elements; thus the quark Lagrangian is given by:

$$\mathcal{L}_{Yq} = -G_d^{i,j}(\bar{u_i}, \bar{d_i'})_L \begin{pmatrix} \phi^+ \\ \phi^0 \end{pmatrix} d_{jR} - G_u^{i,j}(\bar{u_i}, \bar{d_i'})_L \begin{pmatrix} -\bar{\phi}^0 \\ \phi^- \end{pmatrix} u_{jR} + h.c. \tag{2.51}$$

with i,j=1,2,3. After SSB and expansion about the ground state, tha diagonal form of $\mathcal{L}_{Yq}$ is:

$$\mathcal{L}_{Yq} = -m_d^i \bar{d}_i d_i \left(1 + \frac{H}{v}\right) - m_u^i \bar{u}_i u_i \left(1 + \frac{H}{v}\right) \tag{2.52}$$

Fermion masses depend on arbitrary couplings G_l and $G_{u,d}$ and are not predicted by the theory.

2.3.5 The Higgs field

After the characterization of the fermions and gauge bosons as well as their interactions, it is necessary to characterize the Higgs field itself. The Lagrangian $\mathcal{L}_S$ in eqn. 2.36 written in terms of the gauge bosons is given by

$$\mathcal{L}_S = \frac{1}{4}\lambda v^4 + \mathcal{L}_H + \mathcal{L}_{HV} \tag{2.53}$$

$$\mathcal{L}_H = \frac{1}{2}\partial_\mu H \partial^\mu H - \frac{1}{2}m_H^2 H^2 - \frac{1}{2v}m_H^2 H^3 - \frac{1}{8v^2}m_H^2 H^4 \tag{2.54}$$

$$\mathcal{L}_{HV} = m_H^2 W_\mu^+ W^{\mu-} \left(1 + \frac{2}{v}H + \frac{2}{v^2}H^2\right) + \frac{1}{2}m_Z^2 Z_\mu Z^\mu \left(1 + \frac{2}{v}H + \frac{2}{v^2}H^2\right) \tag{2.55}$$

The mass of the Higgs boson is deduced as usual from the mass term in the Lagrangian resulting in:

$$m_H = \sqrt{-2\mu^2} = \sqrt{2\lambda}v \tag{2.56}$$

however, it is not predicted by the theory either. The experimental efforts to find the Higgs boson, carried out by the “Compact Muon Solenoid (CMS)” experiment and the “A Toroidal LHC AppartuS (ATLAS)” experiments at the “Large Hadron Collider(LHC)”, gave great results by July of 2012 when the discovery of a new particle compatible with the Higgs boson predicted by the electroweak theory [39, 40] was announced. Although at the announcement time there were some reservations about calling the new particle the “Higgs boson”, today this name is widely accepted. The Higgs mass measurement, reported by both experiments [41], is in table 2.8.

Property	Value
Electric charge	0
Colour charge	0
Spin	0
Weak isospin	-1/2
Weak hypercharge	1
Parity	1
Mass (GeV/c^2)	125.09±0.21 (stat.)±0.11 (syst.)

Table 2.8: Higgs boson properties. Higgs mass is not predicted by the theory and the value here corresponds to the experimental measurement.

2.3.6 Higgs boson production mechanisms at LHC.

At LHC, Higgs boson is produced as a result of the collision of two counter-rotating protons beams. A detailled description of the LHC machine will be presented in chapter 3. “The total cross section” is a parameter that quantifies the number of pp collisions that happen when a number of protons are fired at each other. Different results can be obtained after a pp collision and for each one the “cross section” is defined as the number of pp collisions that conclude in that particular result with respect to the number of protons fired at each other.

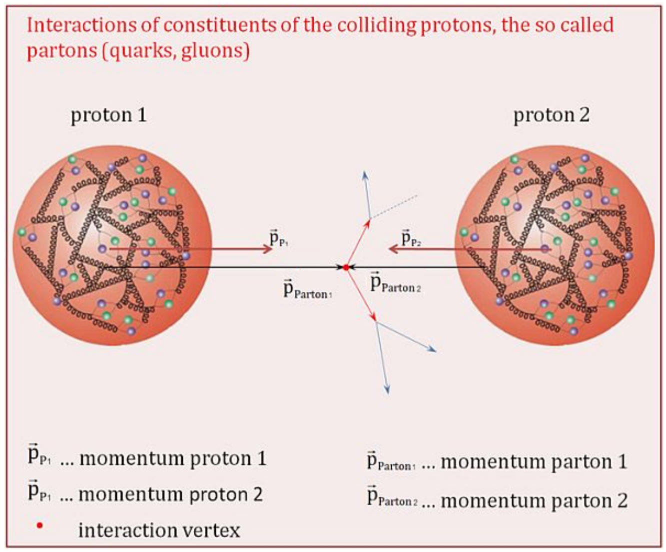

Figure 2.10: Proton-proton collision. Protons are composed of 3 valence quarks, a sea of quarks and gluons; therefore in a proton-proton collision, quarks and gluons are those who collide. [45].

Protons are composed of quarks and these quarks are bound by gluons; however, what is commonly called the quark content of the proton makes reference to the valence quarks. A sea of quarks and gluons is also present inside the proton as represented in figure 2.10. In a proton-proton (pp) collision, the constituents (quarks and gluons) are those who collide. The pp cross section depends on the momentum of the colliding particles, reason for which it is needed to know how the momentum is distributed inside the proton. Quarks and gluons are known as partons and the functions that describe how the proton momentum is distributed among partons inside it are called "parton distribution functions (PDFs)"; PDFs are determined from experimental data obtanied in experiments where the internal structure of hadrons is tested.

In addition, in physics, a common approach to study complex systems consists in starting with a simpler version of them, for which a well known description is available, and add an additional "perturbation" which represents a small deviation from the known behavior. If the perturbation is small enough, the physical quanties associated with the perturbed system are expressed as a series of corrections to those of the simpler system; therefore, the more terms are considered in the series (the higher order in the perturbation series), the more precise is the the description of the complex system.

This thesis explores the Higgs production at LHC; therefore the overview presented here will be oriented specifically to the production mechanisms after pp collisions at LHC.

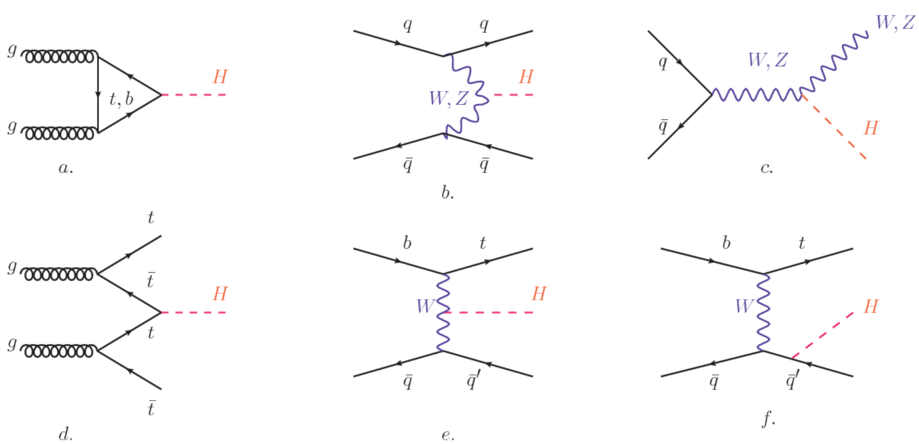

Figure 2.11: Main Higgs production mechanism Feynman diagrams. a. gluon-gluon fusion, b. vector boson fusion (VBF), c. Higgs-strahlung, d. Associated production with a top or bottom quark pair, e-f. associated production with a single top quark.

Figure 2.11 shows the Feynman diagrams for the leading order (first order) Higgs production processes at LHC, while the cross section for Higgs production as a function of the center of mass-energy ($\sqrt{s}$) for pp collisions is showed in figure 2.12 left. The tags NLO (next to leading order), NNLO (next to next to leading order) and N3LO (next to next to next to leading order) make reference to the order at which the pertubation series have been considered.

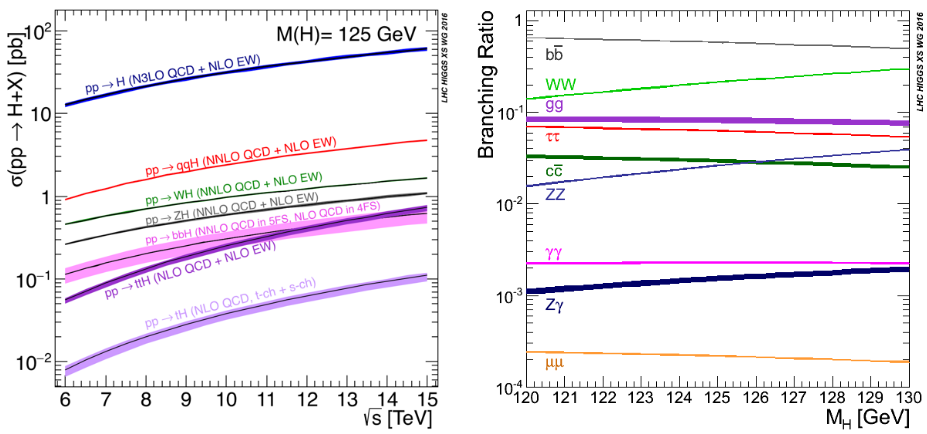

Figure 2.12: Higgs production cross sections (left) and decay branching ratios (right) for the main mechanisms. The VBF is indicated as qqH [42].

As shown in eqns 2.47, 2.51 and 2.55, the strength of the Higgs-fermion interaction is proportional to the fermion mass while the strength of the Higgs-gauge boson interaction is proportional to the square of the gauge boson mass, which implies that the Higgs production and decay mechanisms are dominated by couplings $H-(W,Z,t,b,\tau)$.

The main production mechanism is the gluon fusion (figure 2.11a and $pp \to H$ in figure 2.12) given that gluons carry the highest fraction of momentum of the protons in pp colliders. Since the Higgs boson does not couple to gluons, the mechanism proceeds through the exchange of a virtual top-quark loop given that for it the coupling is the biggest. Note that in this process, the Higgs boson is produced alone, which makes this mechanism experimentally clean when combined with the two-photon or the four-lepton decay channels (see section 2.3.7).

Vector boson fusion (figure 2.11b and $pp \to qqH$ in figure 2.12) has the second largest production cross section. The scattering of two fermions is mediated by a weak gauge boson which later emits a Higgs boson. In the final state, the two fermions tend to be located in a particular region of the detector which is used as a signature when analyzing the datasets provided by the experiments. More details about how to identify events of interest in an analysis will be given in chapter 4.

The next production mechanism is Higgs-strahlung (figure 2.11c and $pp \to WH, pp \to ZH$ in figure 2.12) where two fermions annihilate to form a weak gauge boson. If the initial fermions have enough energy, the emergent boson eventually will emit a Higgs boson.

The associated production with a top or bottom quark pair and the associated production with a single top quark (figure 2.11d-f and $pp \to bbH, pp \to t\bar{t}H, pp \to tH$ in figure 2.12) have a smaller cross section than the main three mechanisms above, but they provide a good opportunity to test the Higgs-top coupling. The analysis reported in this thesis is developed using these production mechanisms. A detailed description of the tH mechanism will be given in section 2.4.

2.3.7 Higgs decay channels

When a particle can decay throught several modes, also known as channels, the probability of decaying throught a given channel is quantified by the "branching ratio (BR)" of the decay channel; thus, the BR is defined as the ratio of number of decays going throught that given channel to the total number of decays. In regard to the Higgs boson decay, the BR can be predicted with accuracy once the Higgs mass is known [43, 44]. In figure 2.12 right, a plot of the BR as a function of the Higgs mass is presented. The largest predicted BR corresponds to the $b\bar{b}$ pair decay channel (see table 2.9).

Decay channel	Branching ratio	Rel. uncertainty
$H \to b\bar{b}$	$5.84 \times 10^{-}1$	$+3.2\% - 3.3\%$
$H \to W^+W^-$	$2.14 \times 10^{-}1$	$+4.3\% - 4.2\%$
$H \to \tau^+\tau^-$	$6.27 \times 10^{-}2$	$+5.7\% - 5.7\%$
$H \to ZZ$	$2.62 \times 10^{-}2$	$+4.3\% - 4.1\%$
$H \to \gamma\gamma$	$2.27 \times 10^{-}3$	$+5.0\% - 4.9\%$
$H \to Z\gamma$	$1.53 \times 10^{-}3$	$+9.0\% - 8.9\%$
$H \to \mu^+\mu^-$	$2.18 \times 10^{-}4$	$+6.0\% - 5.9\%$

Table 2.9: Predicted branching ratios and the relative uncertainty for a SM Higgs boson with $m_H = 125GeV/c^2$. [21]

2.4 Associated Production of Higgs Boson and Single Top Quark.

Associated production of Higgs boson has been extensively studied [46–50]. While measurements of the main Higgs production mechanisms rates are sensitive to the strength of the Higgs coupling to W boson or top quark, they are not sensitive to the relative sign between the two couplings. In this thesis, the Higgs boson production mechanism explored is the associated production with a single top quark (th) which offers sensitiveness to the relative sign of the Higgs couplings to W boson and to top quark. The description given here is based on the reference [48]

A process where two incoming particles interact and produce a final state with two particles can proceed in three ways also called channels (see, for instance, figure 2.13 ommiting the red line). The t-channel represents processes where an intermediate particle is emited by one of the incoming particles and absorbed by the other. The s-channel represents processes where the two incoming particles merge into an intermediate particle which eventually will split into the particles in the final state. The third channel, u-channel, is similar to the t-channel but the two outgoing particles

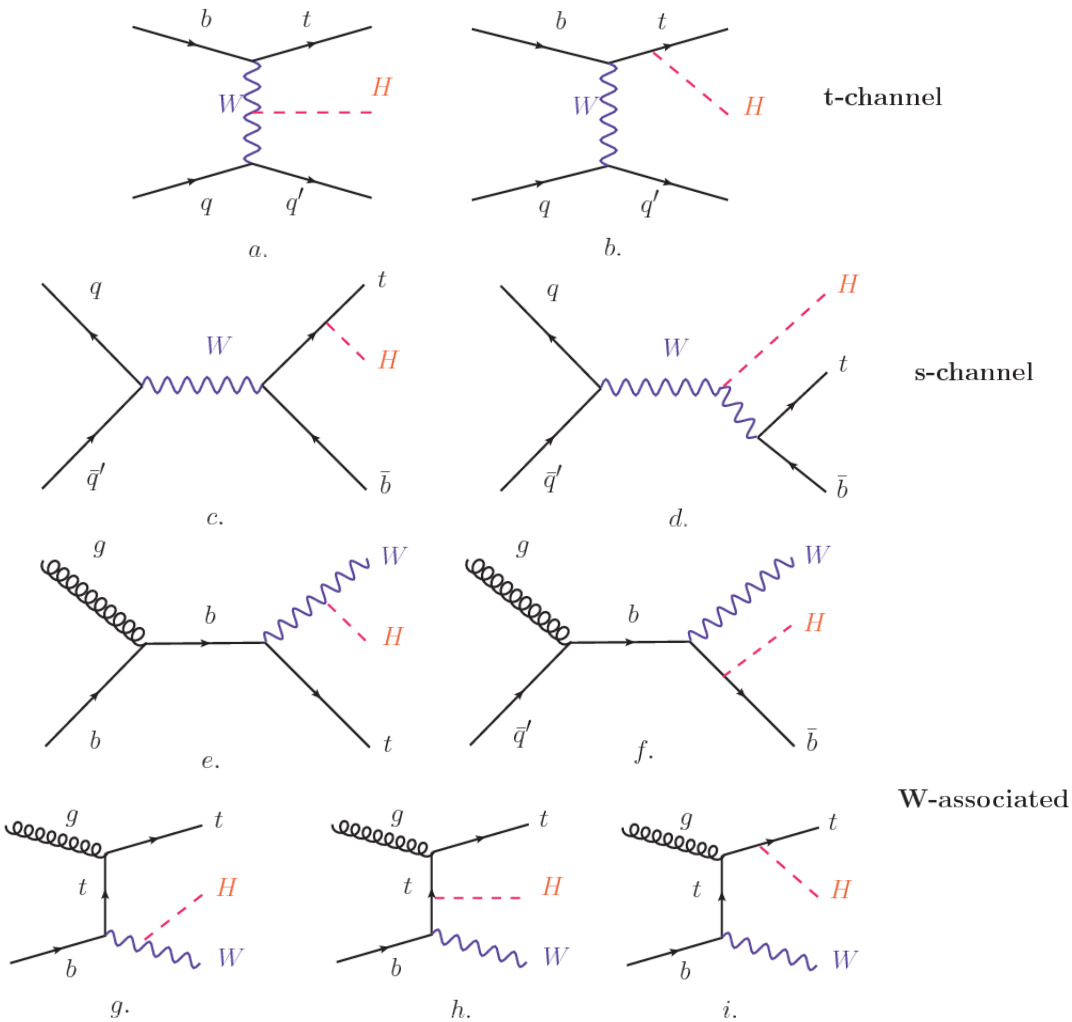

Figure 2.13: Associated higgs production mechanism Feynman diagrams. a.,b. t-channel (tHq), c.,d. s-channel (tHb), e-i. W-associated.

interchange their roles.

The *th* production, where Higgs boson can be radiated either from the top quark or from the W boson, is represented by the leading order Feynman diagrams in figure 2.13. The cross section for the *th* process is calculated, as usual, summing over the contributions from the different feynman diagrams; therefore it depends on the interference between the contributions. In the SM, the interference for t-channel (tHq process) and W-associated (tHW process) production is destructive [46] resulting in the small cross sections presented in table 2.10.

tH production channel	Cross section (fb)
t-channel ($pp \to tHq$)	$70.79^{+2.99}_{-4.80}$
W-associated ($pp \to tHW$)	$15.61^{+0.83}_{-1.04}$
s-channel($pp \to tHb$)	$2.87^{+0.09}_{-0.08}$

Table 2.10: Predicted SM cross sections for tH production at $\sqrt{s} = 13$ TeV [51, 52].

While the s-channel contribution can be neglected, it will be shown that a deviation from the SM destructive interference would result in an enhancement of the th cross section compared to that in SM, which could be used to get information about the sign of the Higgs-top coupling [48, 49]. In order to describe th production processes, Feynman diagram 2.13b will be considered; there, the W boson is radiated by a quark in the proton and eventually it will interact with the b quark. In the high energy regime, the effective W approximation [53] allows to describe the process as the emmision of an approximately on-shell W and its hard scattering with the b quark; i.e. $Wb \to th$. The scattering amplitude for the process is given by

$$\mathcal{A} = \frac{g}{\sqrt{2}}\left[(\kappa_t - \kappa_V)\frac{m_t\sqrt{s}}{m_W v} A\left(\frac{t}{s},\varphi;\xi_t,\xi_b\right) + \left(\kappa_V \frac{2m_W}{v}\frac{s}{t} + (2\kappa_t - \kappa_V)\frac{m_t^2}{m_W v}\right) B\left(\frac{t}{s},\varphi;\xi_t,\xi_b\right)\right], \tag{2.57}$$

where $\kappa_V \equiv g_{HVV}/g_{HVV}^{SM}$ and $\kappa_t \equiv g_{Ht}/g_{Ht}^{SM} = y_t/y_t^{SM}$ are scaling factors that quantify possible deviations of the couplings, Higgs-Vector boson (H-W) and Higgs-top (H-t) respectively, from the SM couplings; $s = (p_W + p_b)^2$, $t = (p_W - p_H)^2$, φ is the Higgs azimuthal angle around the z axis taken parallel to the direction of motion of the incoming W; A and B are funtions describing the weak interaction in terms of the chiral states of the quarks b and t. Terms that vanish in the high energy limit have been neglected as well as the Higgs and b quark masses[8].

The scattering amplitude grows with energy like $\sqrt{s}$ for $\kappa_V \neq \kappa_t$, in contrast to the SM ($\kappa_t = \kappa_V = 1$), where the first term in 2.57 cancels out and the amplitude is constant for large s; therefore, a deviation from the SM predictions represents an enhancement in the tHq cross section. In particular, for a SM H-W coupling and a H-t coupling of inverted sigh with respect to the SM ($\kappa_V = -\kappa_t = 1$) the tHq cross section is enhanced by a factor greater 10 as seen in the figure 2.14 taken from reference [48]; reference [54] has reported similar enhancement results.

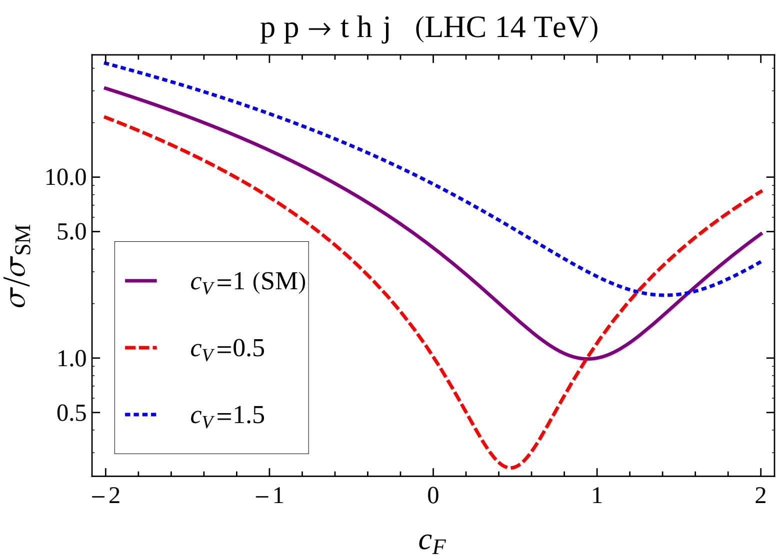

Figure 2.14: Cross section for tHq process as a function of κ_t, normalized to the SM, for three values of κ_V. In the plot c_f refers to the Higgs-fermion coupling which is dominated by the H-t coupling and represented here by κ_t. Solid, dashed and dotted lines correspond to $c_V \to \kappa_V = 1, 0.5, 1.5$ respectively. Note that for the SM ($\kappa_V = \kappa_t = 1$), the destructive effect of the interference is maximal.

A similar analysis is valid for the W-associated channel but, in that case, the interference is more complicated since there are more than two contributions and an ad-

[8] A detailed explanation of the structure and approximations used to derive $\mathcal{A}$ can be found in reference [48]

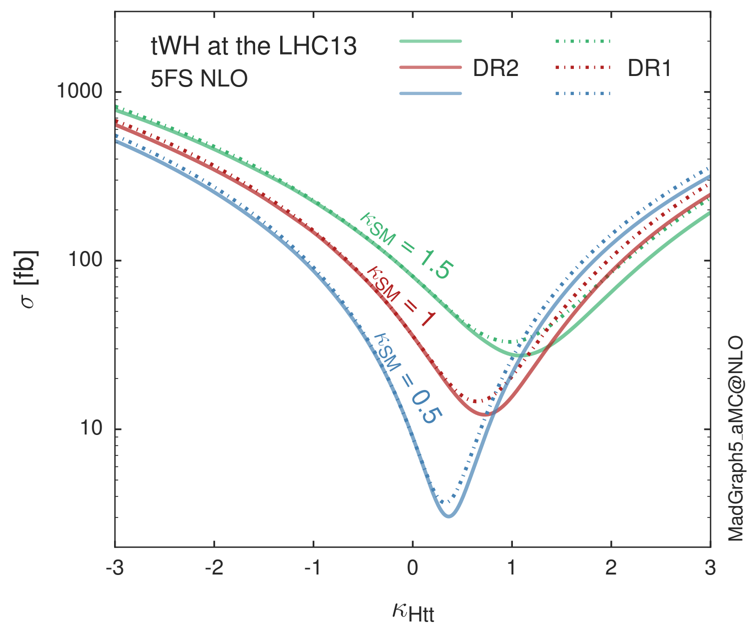

Figure 2.15: Cross section for tHW process as a function of κ_{Htt}, for three values of κ_{SM} at $\sqrt{s} = 13$ TeV. $\kappa^2_{Htt} = \sigma_{Htt}/\sigma^{SM}_{Htt}$ is a simple rescaling of the SM Higgs interactions.

ditional interference with the production of Higgs boson and a top pair process($t\bar{t}H$). The calculations are made using the so-called Diagram Removal (DR) technique where interfering diagrams are removed (or added) from the calculations in order to evaluate the impact of the removed contributions. DR1 was defined to neglect $t\bar{t}H$ interference while DR2 was defined to take $t\bar{t}H$ interference into account [55]. As shown in figure 2.15, the tHW cross section is enhanced from about 15 fb (SM: $\kappa_{Htt} = 1$) to about 150 fb ($\kappa_{Htt} = -1$). Differences between curves for DR1 and DR2 help to gauge the impact of the interference with $t\bar{t}H$.

Results of the calculations of the tHq and tHW cross sections at $\sqrt{s} = 13$ TeV can be found in reference [56] and a summary of the results is presented in table 2.11.

	$\sqrt{s}$ TeV	$\kappa_t = 1$	$\kappa_t = -1$
$\sigma^{LO}(tHq)$(fb) [48]	8	≈ 17.4	≈ 252.7
	14	≈ 80.4	≈ 1042
$\sigma^{NLO}(tHq)$(fb) [48]	8	$18.28^{+0.42}_{-0.38}$	$233.8^{+4.6}_{-0.0}$
	14	$88.2^{+1.7}_{-0.0}$	$982.8^{+28}_{-0.0}$
$\sigma^{LO}(tHq)$(fb) [54]	14	≈ 71.8	≈ 893
$\sigma^{LO}(tHW)$(fb) [54]	14	≈ 16.0	≈ 139
$\sigma^{NLO}(tHq)$(fb) [56]	8	$18.69^{+8.62\%}_{-17.13\%}$	-
	13	$74.25^{+7.48\%}_{-15.35\%}$	$848^{+7.37\%}_{-13.70\%}$
	14	$90.10^{+7.34\%}_{-15.13\%}$	$1011^{+7.24\%}_{-13.39\%}$
$\sigma^{LO}(tHW)$(fb) [55]	13	$15.77^{+15.91\%}_{-15.76\%}$	-
$\sigma^{NLO}DR1(tHW)$(fb) [55]	13	$21.72^{+6.52\%}_{-5.24\%}$	≈ 150
$\sigma^{NLO}DR2(tHW)$(fb) [55]	13	$16.28^{+7.34\%}_{-15.13\%}$	≈ 150

Table 2.11: Predicted enhancement of the tHq and tHW cross sections at LHC for $\kappa_V = 1$ and $\kappa_t = \pm 1$ at LO and NLO; the cross section enhancement of more that a factor of 10 is due to the flippling in the sign of the H-t coupling with respect to the SM one.

2.5 The CP-mixing in tH processes

In addition to the sensitivity to sign of the H-t coupling, tHq and tHW processes have been proposed as a tool to investigate the possibility of a H-t coupling that does not conserve CP [50, 55, 57]. Current experimental results are consistent with SM H-V and H-t couplings; however, negative H-t coupling is not excluded completely [59].

In this thesis, the sensitivity of th processes to CP-mixing is also studied in the effective field theory framework and based in references [50, 55]; a generic particle (X_0) of spin-0 and a general CP violating interaction with the top quark, can couple to scalar and pseudoscalar fermionic densities. The H-W interaction is assumed to be SM-like. The Lagrangian modeling the H-t interaction is given by

$$\mathcal{L}_0^t = -\bar{\psi}_t \left(c_\alpha \kappa_{Htt} g_{Htt} + i s_\alpha \kappa_{Att} g_{Att} \gamma_5 \right) \psi_t X_0, \tag{2.58}$$

where α is the CP-mixing phase, $c_\alpha \equiv \cos\alpha$ and $s_\alpha \equiv \sin\alpha$, κ_{Htt} and κ_{Att} are real dimensionless rescaling parameters[9], $g_{Htt} = g_{Att} = m_t/v = y_t/\sqrt{2}$ and $v \sim 246$ GeV is the Higgs vacuum expectation value. In this parametrization, it is easy to recover three special cases

- CP-even coupling $\rightarrow \alpha = 0^o$
- CP-odd coupling $\rightarrow \alpha = 90^o$
- SM coupling $\rightarrow \alpha = 0^o$ and $\kappa_{Htt} = 1$

The loop induced X_0 coupling to gluons can also be described in terms of the parametrization above, according to

$$\mathcal{L}_0^g = -\frac{1}{4}\left(c_\alpha \kappa_{Hgg} g_{Hgg} G^a_{\mu\nu} G^{a,\mu\nu} + s_\alpha \kappa_{Agg} g_{Agg} G^a_{\mu\nu} \widetilde{G}^{a,\mu\nu}\right) X_0. \tag{2.59}$$

where $g_{Hgg} = -\alpha_s/3\pi v$ and $g_{Agg} = \alpha_s/2\pi v$. Under the assumption that the top quark dominates the gluon-fusion process at LHC energies, $\kappa_{Hgg} \rightarrow \kappa_{Htt}$ and $\kappa_{Agg} \rightarrow \kappa_{Att}$, so that the ratio between the gloun-gluon fusion cross section for X_0 and for the SM Higgs prediction can be written as

$$\frac{\sigma_{NLO}^{gg\rightarrow X_0}}{\sigma_{NLO,SM}^{gg\rightarrow H}} = c_\alpha^2 \kappa_{Htt}^2 + s_\alpha^2 \left(\kappa_{Att} \frac{g_{Agg}}{g_{Hgg}}\right)^2. \tag{2.60}$$

If the rescaling parameters are set to

$$\kappa_{Htt} = 1, \qquad \kappa_{Att} = \left|\frac{g_{Hgg}}{g_{Agg}}\right| = \frac{2}{3}. \tag{2.61}$$

the gluon-fusion SM cross section is reproduced for every value of the CP-mixing angle α; therefore, by imposing that condition to the Lagrangian density 2.58, the

[9] analog to κ_t and κ_V

CP-mixing angle is not constrained by current data. Figure 2.16 shows the NLO cross sections for t-channel tX_0(blue) and $t\bar{t}X_0$ (red) associated production processses as a function of the CP-mixing angle α. X_0 is a generic spin-0 particle with top quark CP-violating coupling. Rescaling factors κ_{Htt} and κ_{Att} have been set to reproduce the SM gluon-fusion cross sections.

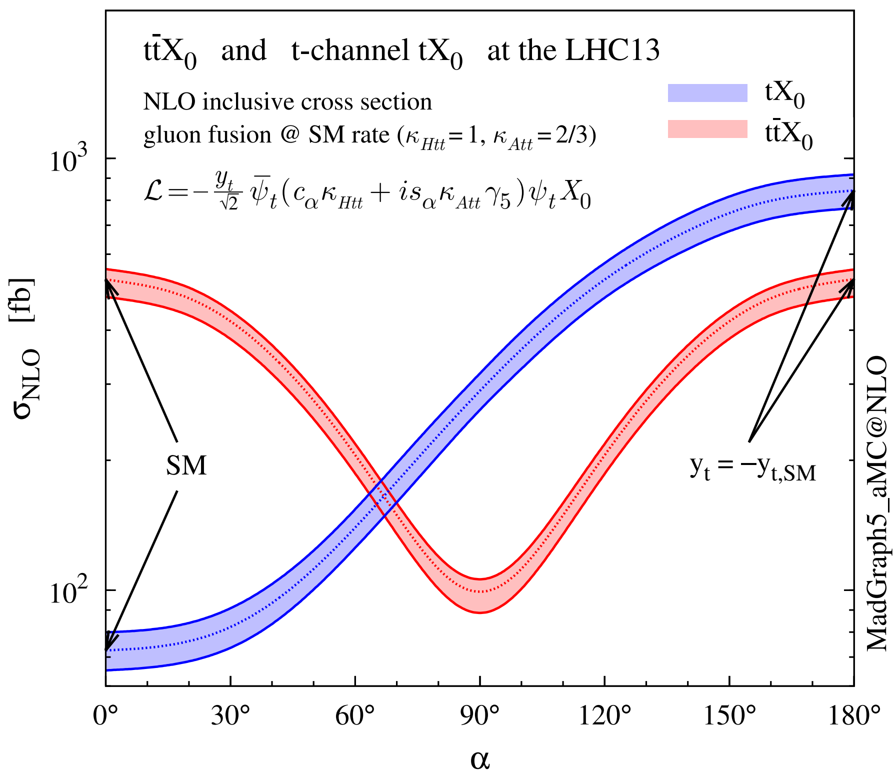

Figure 2.16: NLO cross sections for t-channel tX_0(blue) and $t\bar{t}X_0$ (red) associated production processses as a function of the CP-mixing angle α. X_0 is a generic spin-0 particle with top quark CP-violating coupling [50].

It is interesting to notice that the tX_0 croos section is enhanced, by a factor of about 10, when a continuous rotation in the scalar-pseudoscalar plane is applied; this enhancement is similar to the enhancement produced when the H-t coupling is flipped in sign with respect to the SM ($y_t = -y_{t,SM}$ in the plot), as showed in section 2.4. In contrast, the degeneracy in the $t\bar{t}X_0$ cross section is still present given that it depends quadratically on the H-t coupling, but more insterting is to notice that $t\bar{t}X_0$ cross section is exceeded by tX_0 cross section after $\alpha \sim 60^o$.

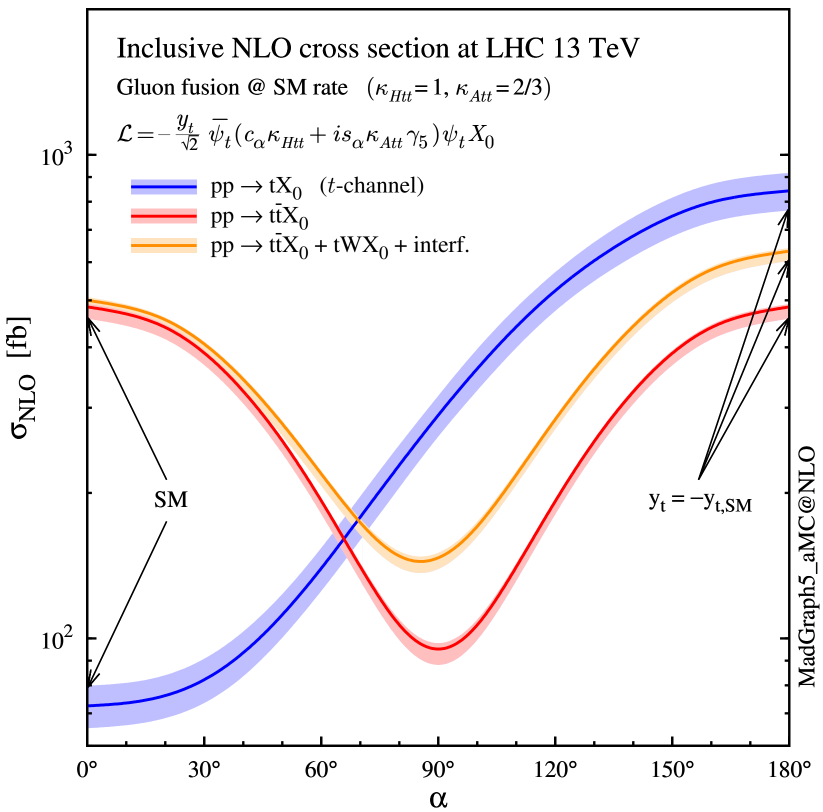

Figure 2.17: NLO cross sections for t-channel tX_0(blue), $t\bar{t}X_0$ (red) associated production processses and combined $tWX_0 + t\bar{t}X_0$ (including interference) production as a function of the CP-mixing angle α [50].

A similar parametrization can be used to investigate the tHW process sensitivity to CP-violating H-t coupling. As said in 2.4, the interference in the W-associated channel is more complicated because there are more than two contributions and also there is interference with the $t\bar{t}H$ production process.

Figure 2.17 shows the NLO cross sections for t-channel tX_0(blue), $t\bar{t}X_0$ (red) associated production and for the combined $tWX_0 + t\bar{t}X_0+$ interference (orange) as a function of the CP-mixing angle. It is clear that the effect of the interference in the combined case is the lifting of the degeneracy present in the $t\bar{t}X_0$ production. The constructive interference enhances the cross section from about 500 fb at SM ($\alpha = 0$) to about 600 fb ($\alpha = 180^o \rightarrow y_t = -y_{t,SM}$).

An analysis combining tHq and tHW processes will be made in this thesis taking advantage of the sensitivity improvement.

2.6 Experimantal status of anomalous Higg-fermion coupling.

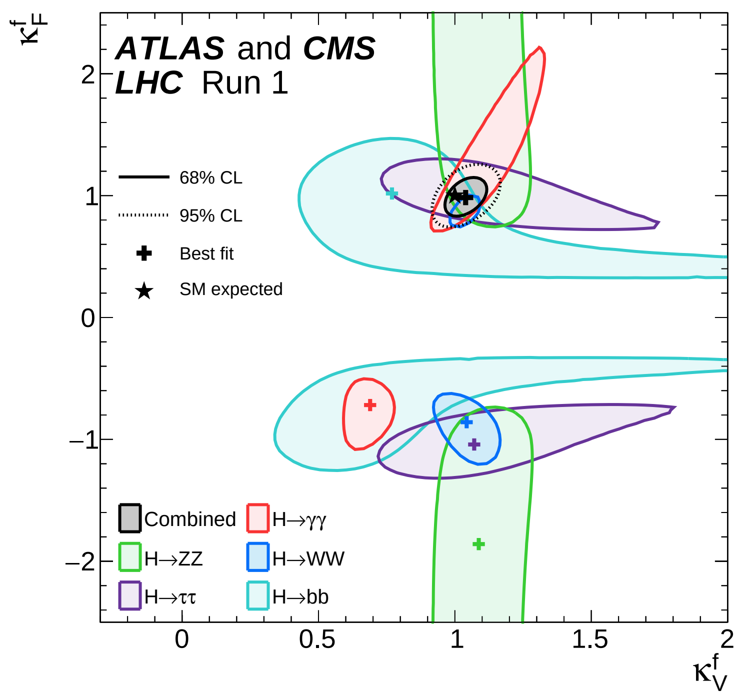

Figure 2.18: Combination of coupling modifiers κ_t-κ_V fits of ATLAS and CMS; also shown the individual decay channels combination and their global combination. No assumptions have been made on the sign of the coupling modifiers [59].

ATLAS and CMS have performed analysis of the anomaloun H-f coupling by making likelihood scans for the two coupling modifiers, κ_t and κ_V, under the assumption that

$\kappa_Z = \kappa_W = \kappa_V$ and $\kappa_t = \kappa_\tau = \kappa_b = \kappa_f$. Figure2.18 shows the result of the combination of ATLAS and CMS fits; also the individual decay channels combination and the global combination result are shown.

While all the channels are compatible for positive values of the modifiers, for negative values of κ_t there is no compatibility. The best fit for individual channels is compatible with negative values of κ_t except for the $H \to bb$ channel which is expected to be the most sensitive channel; therefore, the best fit for the global fit yields $\kappa_t \geq 0$. Thus, the annomaluos H-t coupling cannot be excluded completely.

Chapter 3

The CMS experiment at the LHC

3.1 Introduction

Located in the Swiss-French border, the European Council for Nuclear Research (CERN) is the largest scientific organization leading the particle physics research. About 13000 people in a broad range of fields including users, students, scientists, engineers among others, contribute to the data taking and analysis, with the goal of unveiling the secrets of the nature and revealing the fundamental structure of the universe. CERN is also the home of the Large Hadron Collider (LHC), the largest circular particle accelerator around the world, where protons (or heavy ions) traveling close to the speed of light, are made to collide. These collisions open a window to investigate how particles (and their constituents if they are composite) interact with each other, providing clues about the laws of the nature. This chapter present an overview of the LHC structure and operation. A detaled description of the CMS detector is offered, given that the data used in this thesis have been taken with this detector.

3.2 The LHC

With 27 km of circumference, the LHC is currently the largest and most powerful accelerator in the world. It is installed in the same tunnel where the large Electron-Positron (LEP) collider was located, taking advantage of the existing infraestructure. The LHC is also the larger accelerator in the CERN's accelerator complex and is assisted by several successive accelerating stages before the particles are injected into the LHC ring where they reach their maximum eneregy (see figure 3.1).

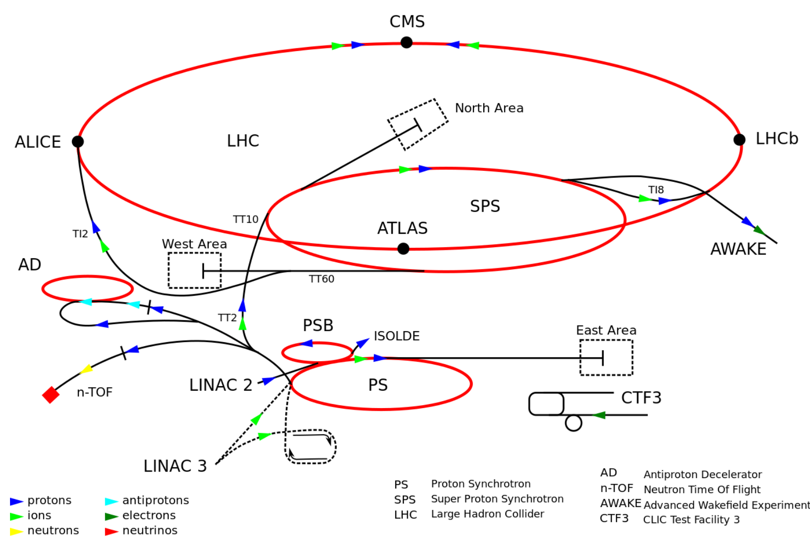

Figure 3.1: CERN accelerator complex. Blue arrows show the path followed by protons along the acceleration process [60].

LHC run in three modes depending on the particles being accelerated

- Proton-Proton collisions (pp) for multiple physics experiments.
- Lead-Lead collisions (Pb-Pb) for heavy ion experiments.
- Proton-Lead collisions (p-Pb) for quark-gluon plasma experiments.

In this thesis pp collisions will be considered.

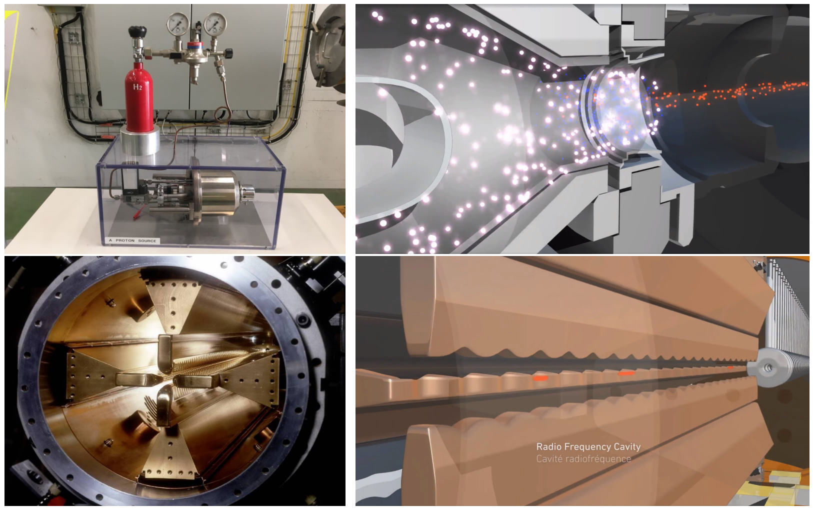

Figure 3.2: LHC protons source and first acceleration stage. Top: the bottle contains hydrogen gas (white dots) which is injected into the metal cylinder to be broken down into electrons(blue dots) and protons(red dots); Bottom: the obtained protons are directed towards the radio frequency quadrupole which perform the first acceleration, focus the beam and create the bunches of protons. [64, 65]

Collection of protons starts with hydrogen atoms taken from a bottle, containing hydrogen gas, and injecting them in a metal cillinder; hydrogen atoms are broken down into electrons and protons by an intense electric field (see figure3.2 top). The resulting protons leave the metal cylinder towards a radio frecuency quadrupole (RFQ) that focus the beam, accelerate the protons and create the packets of protons called bunches. In the RFQ, an electric field is generated by a RF wave at a frecuency that matches the resonance frecuency of the cavity where the electrodes are contained. The beam of protons traveling on the RFQ axis experience an alternating electric field gradient that generates the focusing forces.

In order to accelerate the protons, a longitudinal time-variying electric field component is added to the system; it is done by giving the electrodes a sinus-like profile as shown in figure 3.2 bottom. By matching the speed and phase of the protons with the longitudinal electric field the bunching is performed; protons synchronized with the

RFQ (synchronous proton) does not feel an accelerating force, but those protons in the beam that have more (or less) energy than the synchronous proton (asynchronous protons) will feel a decelerating (accelerating) force; therefore, asynchronous protons will oscillate around the synchronous ones forming bunches of protons [62]. From the RFQ emerges protons with energy 750 keV in bunches of about 1.15×10^{11} protons [63].

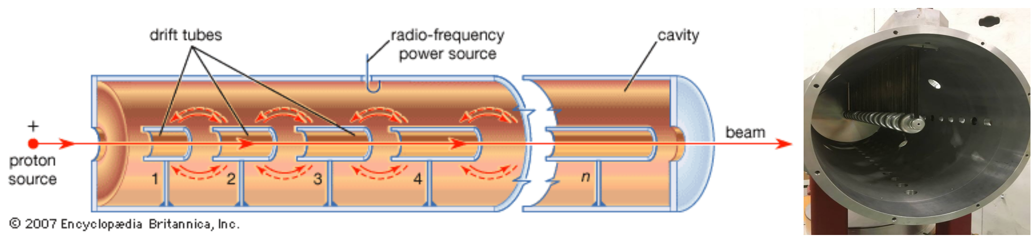

Figure 3.3: The LINAC2 accelerating system at CERN. Radio frecuency (RF) generated electric fields create acceleration and deceleration zones inside the cavity; deceleration zones are blocked by drift tubes where quadrupole magnets focus the proton beam. [66]

Proton bunches coming from the RFQ goes to the linear accelerator 2 (LINAC2) where they are accelerated to reach 50 MeV energy. In the LINAC2 stage, acceleration is performed using radio frecuency generated electric fields which create zones of acceleration and deceleration as shown in figure 3.3. In the decelerations zones the electric field is blocked using drift tubes where protons are free to drift while quadrupole magnets focus the beam.

The beam coming from LINAC2 is injected into the proton synchrotron booster (PSB) to reach 1.4 GeV in energy. The next acceleration is provided at the proton synchrotron (PS) up to 26 GeV, followed by the injection into the super proton synchrotron (SPS) where protons are accelerated to 450 GeV. Finally, protons are injected into the LHC where they are accelerated to the target energy of 6.5 TeV. PSB, PS, SPS and LHC accelerate protons using the same RF acceleration technic described before.

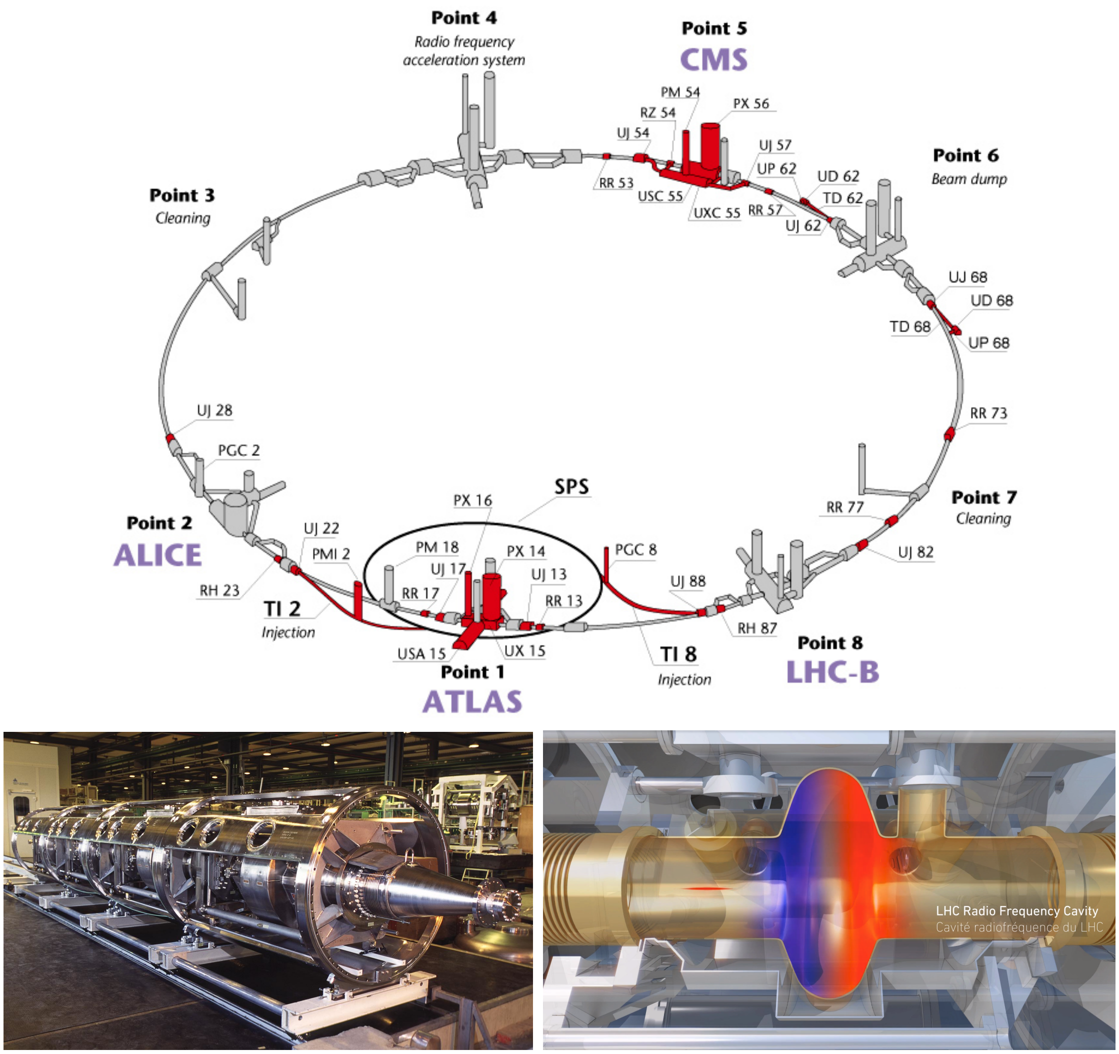

Figure 3.4: Top: LHC layout. The red zones indicate the infrastructure additions to the LEP installations, built to accomodate the ATLAS and CMS experiments which exceed the size of the former experiments located there [61]. Bottom: LHC RF cavities. A module accomodates 4 cavities that accelerate protons and preserve the bunch structure of the beam. [65, 67]

LHC have a system of 16 RF cavities located in the so-called point 4, as shown in figure 3.4 top, tunned at a frecuency of 400 MHz and the protons are carefully timed so additionally to the acceleration effect the bunch structure of the beam is preserved. Bottom side of figure 3.4 shows a picture of a Rf module composed of 4 RF cavities working in a superconducting state at 4.5 K; also is showed a representation of the accelerating electric field that accelerates the protons in the bunch.

While protons are accelerated in one section of the LHC ring, where the RF cavities are located, in the rest of their path they have to be kept in the curved trajectory defined by the LHC ring. Technically, LHC is not a perfect circle; RF, injection, beam dumping, beam cleaning and sections before and after the experimental points where protons collide are all straight sections. In total, there are 8 arcs 2.45 Km long each and 8 straight sections 545 m long each. In order to curve the proton's trajectory in the the arc sections, superconducting dipole magnets are used.

Inside the LHC ring, there are two proton beams traveling in opposite directions in two separated beam pipes; the beam pipes are kept at ultra high vacuum ($\sim 10^{-9}$ Pa) to ensure that there are no particles that interact with the proton beams. The superconducting dipole magnets used in LHC are made of a NbTi alloy, capable of transporting currents of about 12000 A when cooled at a temperature below 2K using liquid helium (see figure 3.5).
Protons in the arc sections of LHC feel a centripetal force exerted by the dipole magnets which is perpendicular to the beam trajectory; The magnitude of magnetic field needed can be found assuming that protons travel at $v \approx c$, using the standard values for proton mass and charge and the LHC radius, as

$$F_m = \frac{mv^2}{r} = qBv \quad \rightarrow B = 8.33T \tag{3.1}$$

wich is about 100000 times the Earth's magnetic field. A representation of the magnetic field generated by the dipole magnets is shown in the bottom left side of figure

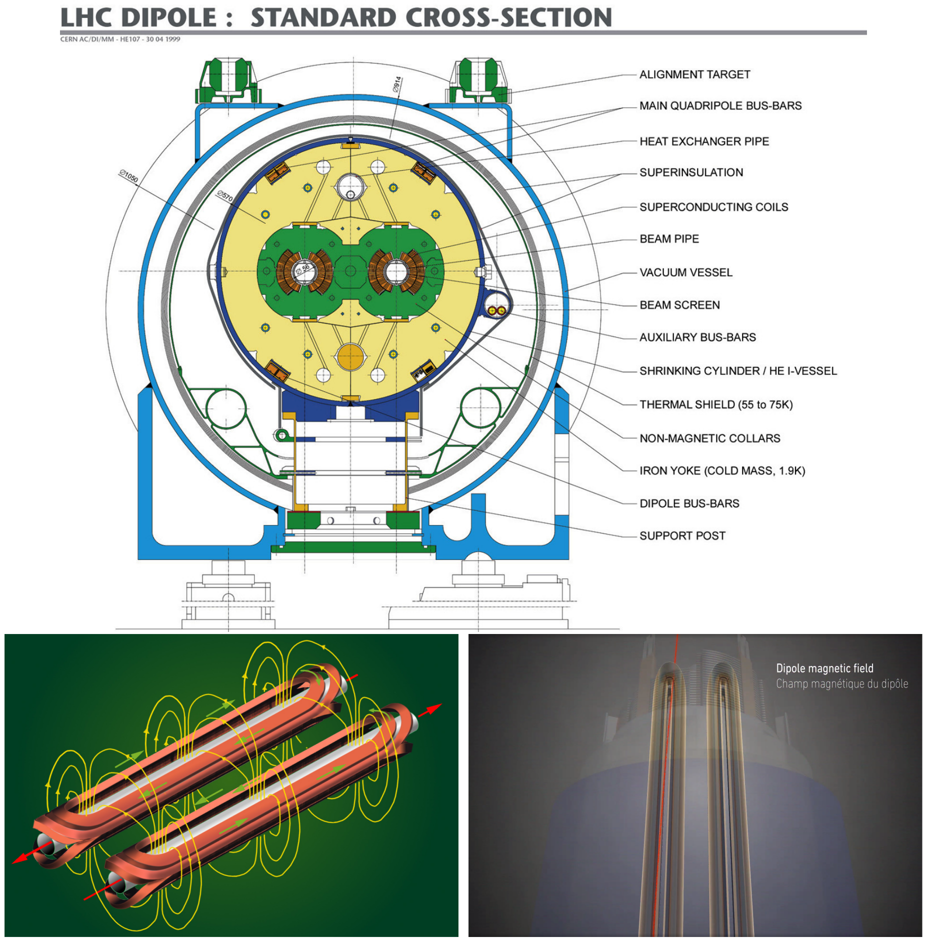

Figure 3.5: Top: LHC dipole magnet transversal view; cooling, shielding and mechanical support are indicated. Bottom left: Magnetic field generated by the dipole magnets; note that the direction of the field inside one beam pipe is opposite with respect to the other beam pipe which guarantee that both proton beams are curved in the same direction towards the ceneter of the ring. The effect of the dipole magnetic field on the proton beam is represented in the bottom right side [65, 68, 69].

3.5. The bending effect of the magnetic field on the proton beam is shown in the bottom right side of figure 3.5. Note that the dipole magnets are not curved; the arc section of the LHC ring is composed of straight dipole magnets of about 15 m. In total there are 1232 dipole magnets along the LHC ring.

In addition to bending the beam trajectory, the beam has to be focused so it stays in side the beam pipe. The focusing is performed by quadrupole magnets installed in another straight section; in total 858 quadrupole magnets are installed along the LHC ring. Other effects like electromagnetic interaction among bunches, interaction with electron clouds from the beam pipe, gravitational force on the protons, differences in energy among protons in the same bunch, among others, are corrected using sextupole and other magnetic multipoles.

The two proton beams inside the LHC ring are made of bunches with a cylindrical shape of about 7.5 cm long and about 1 mm in diameter; when bunches are close to the collision point (IP), the beam is focused up to a diameter of about 16 μm in order to maximize the luminosity (L) defined as the number of collisions per unit area and per second. Luminosity can be calculated using

$$L = fn\frac{N_1 N_2}{4\pi\sigma_x\sigma_y} \tag{3.2}$$

where f is the revolution frecuency, n is the number of bunches per beam, N_1 and N_2 are the number of protons per bunch, σ_x and σ_y are the gaussian transverse sizes of the bunches. Using

$$\begin{aligned} f =& \frac{v}{2\pi r_{LHC}} \approx \frac{3\times10^8 m/s}{27km} \approx 11.1kHz, \\ n =& 2808 \\ N_1 =& N_2 = 1.5\times10^{11} \\ \sigma_x =& \sigma_y = 16\mu m \end{aligned}$$

$$L = 1.28\times10^{34}cm^{-2}s^{-1} \tag{3.3}$$

Luminosity is a fundamental aspect for LHC given that the bigger luminosity, the bigger number of collisions, which means that for processes with a very small cross section the number of expected occurrencies is increased and so the chances of being detected. The integrated luminosty collected by the CMS experiment during 2016 is shown in figure 3.6; the data analized in this thesis corresponds to an integrated luminosity of 35.9 fb^{-1} at $\sqrt{s} = 13$ TeV.

A way to increase L is increasing the number of bunches in the beam. Currently, the separation between two consecutive bunches in the beam is 7.5 m which corresponds to a time separation of 25 ns. In the full LHC ring the allowed number of bunches is $n = 27km/7.5m = 3600$; however, there are some gaps in the bunch pattern intended for preparing the dumping and injection of the beam, thus, the proton beams are composed of 2808 bunches.

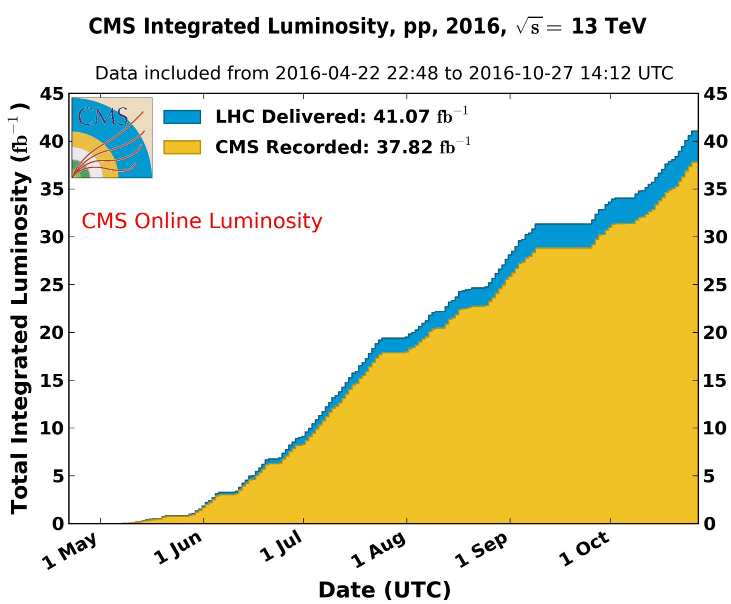

Figure 3.6: Integrated luminosity delivered by LHC and recorded by CMS during 2016. The difference between the delivered and the recorded luminosities is due to fails and issues occured during the data taking in the CMS experiment [70].

Once the proton beams reach the desired energy, they are brought to cross each other producing proton-proton collisions. The bunch crossing happens in precise places where the four LHC experiments are located, as seen in figure 3.7 left. In 2008, the first set of collisions involved protons with $\sqrt{s} = 7$ TeV; the energy was increased to 8 TeV in 2012 and to 13 TeV in 2015.

CMS and ATLAS experiments, which are multi-purpose experiments, are enabled to explore physics in any of the collision modes. LHCb experiment is optimized to explore botom quark physics, while ALICE is optimized for heavy ion collisions searches; TOTEM and LHCf are dedicated to forward physics studies; MoEDAL (not indicated in the figure) is intended for monopoles or massive pseudo stable particles searches.

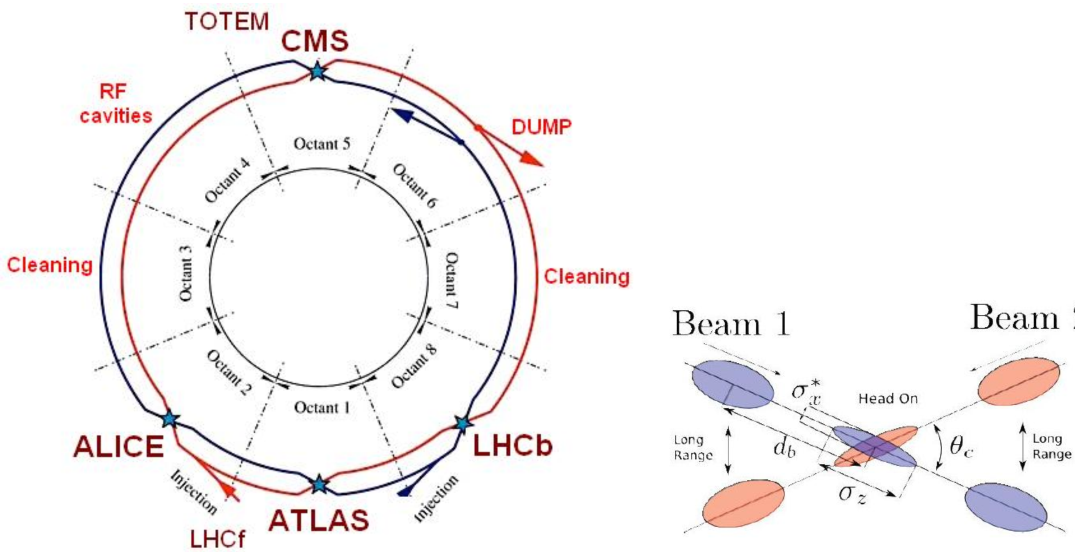

Figure 3.7: Left: LHC interaction points. Bunch crossing occurs where the LHC experiments are located [71]. Sections indicated as cleaning are dedicated to collimate the beam in order to protect the LHC ring from collisions with protons in very spreaded bunches. Right: bunch crossing scheme. Since the bunch crossing is not perfectly head-on, the luminosity is reduced in a factor of 17%.

At the IP there are two interesting details that need to be addressed. The first one is that the bunch crossing does not occur head-on but at a small crossing angle (280 μrad in CMS and ATLAS) as shown in the right side of figure 3.7, affecting the overlapping between bunches; the consecuence is a reduction of about 17% in the luminosity. The second one is occurence of multiple pp collisions in the same bunch crossing; this effect is called pile-up (PU). A fairly simple estimation of the PU follows from estimating the probability of collision between two protons, one from each of the bunches in course of collision; it depends roughly on the ratio of proton size and the cross section of the bunch in the interaction point, i.e.,

$$P(pp-collision) \sim \frac{d^2_{proton}}{\sigma_x \sigma_y} = \frac{(1fm)^2}{(16\mu m)^2} \sim 4 \times 10^{-21} \quad (3.4)$$

however, there are $N = 1.15 \times 10^{11}$ protons in a bunch, thus the estimated number of collisions in a bunch crossing is

$$PU = N^2 * P(pp-collision) \sim 50 \text{ pp-collision per bunch crossing.} \quad (3.5)$$

Each collision geenerates a vertex, but only the most energetic is considered as a primary vertex and the rest are considered as PU vertices. A simulation of a multiple pp collision event in a bunch crossing at CMS is showed in figure3.8. Unstable particles outgoing from the primary vertex will eventually decay; this decay vertex is knon as a secondary vertex.

When the beams are exhausted, i.e. the number of protons in the bunches is reduced beyond a limit, or in case of emergency, the beams have to be extracted from the beam pipes; the dumping system, in the dump section, perform the extraction safely by directing the beams towards graphite blocks that absorb the beam energy.

Next section present a description of the CMS detector, since it is the detector used to collect the data used in this thesis.

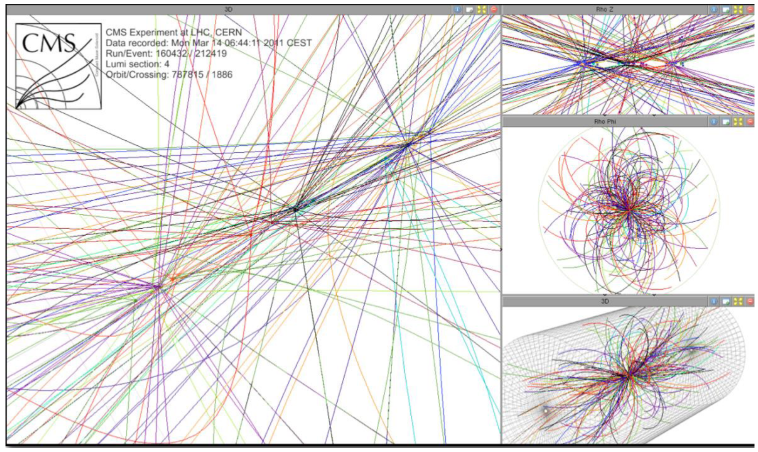

Figure 3.8: Multiple pp collision bunch crossing at CMS. Only the most energetic vertex is considered and the rets are cataloged as PU vertices [].

3.3 The CMS experiment

CMS is a general purpose detector designed to conduct research in a wide range of physics from standard model to new physics like extra dimensions and dark matter. Located at the point 5 in the LHC layout as shown in figure 3.4, CMS is composed of several detection systems distributed in a cylindrical structure,. In total, CMS weight about 12500 tons in a very compact 21.6 m long and 14.6 m diameter cylinder. It was built in 15 separated sections at the ground level and lowered to the cavern individually to be assembled. A complete and detailed description of the CMS detector and its components is given in reference [72] on which this section is based in.

Figure 3.9 shows the layout of the CMS detector. The design is driven by the requirements on the identification, momentum resolution and unambiguous charge determination of the muons; therefore, a large bending power is provided by the solenoid magnet made of superconducting cable capable to generate a 3.8 T magnetic field. The detection system is comppposed of (from the innermost to the outermost)

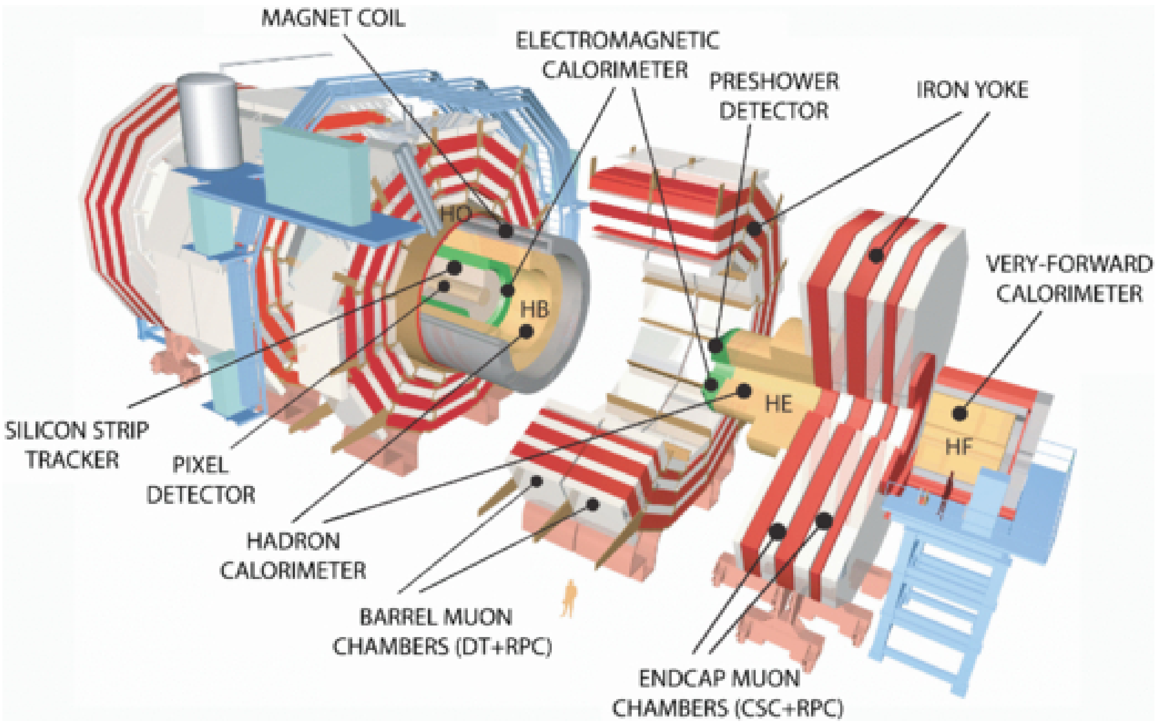

Figure 3.9: CMS detector drawing [73].

- Pixel detector.
- Silicon strip tracker.
- Preshwoer detector.
- Electromagnetic calorimeter.
- Hadronic calorimeter.
- Muon chambers (Barrel and endcap)

3.3.1 Coordinate system

The coordinate system used by CMS is centerd in the geometrical center of the detector which is the same as the IP as shown in figure3.10. The z-axis is parallel to the beam direction, while the Y-axis pointing vertically upward, and the X-axis pointing radially inward toward the center of the LHC.

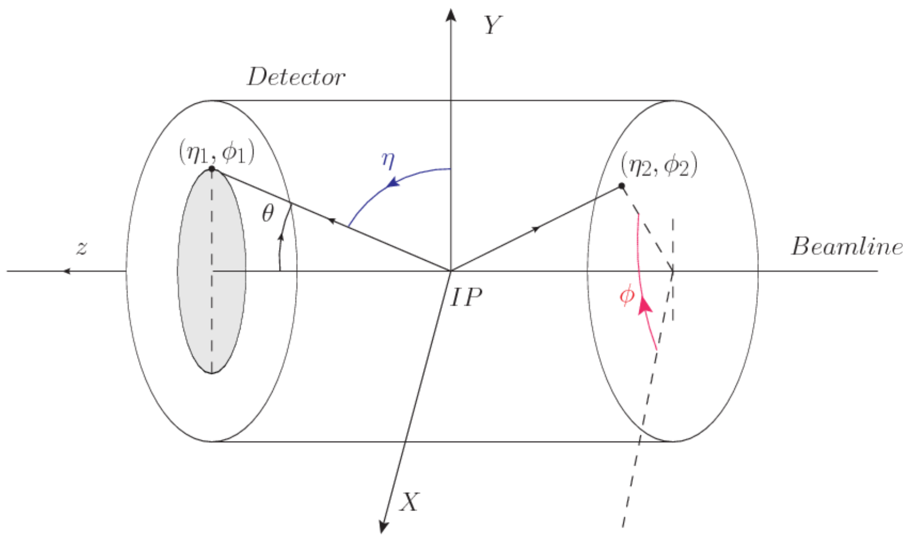

Figure 3.10: CMS coordinate system.

In addition to the common cartesian and cylindrical coordinate systems, two coordinates are of particular utility in particle physics: rapidity(y) and pseudorapidity(η), defined in conection to the polar angle θ, energy and longitudinal momentum component (momentum along the z-axis) according to

$$y = \frac{1}{2} ln \frac{E + p_z}{E - p_z} \qquad \eta = -ln \left(tan \frac{\theta}{2} \right) \tag{3.6}$$

Rapidity is related to the angle between the XY-plane and the direction in which the products of a collision are emitted; it has the nice property that the difference between the rapidities of two particles is invariant with respect to Lorents boosts along the z-axis. Thus, data analysis becomes more simple when based in rapidity; however, it is not simple to measure the rapidity of higly relativistic particles, as those produced after pp collisions. Under the highly relativistic motion approximation y can be rewritten in terms of the polar angle, arriving to the conclusion that rapidity is approximately equal to the pseudorapidity defined above, i.e. $y \approx \eta$. Note that η is easier to measure that y given the direct relationship between the former and the polar angle. Angular distance between two objects in the detector (ΔR) is defined in terms of their coordinates (η_1, ϕ_1), (η_2, ϕ_2) as

$$\Delta R = \sqrt{(\Delta\eta)^2 - (\Delta\phi)^2} \tag{3.7}$$

3.3.2 Pixels detector

The CMS tracking system is designed to provide a precise measurement of the trajectory followed by the charged particles created after the pp collisions as; also, the the precise reconstruction of the primary and secondary vertices is expected. In a bunch crossing, it is expected that about 50 there will be about 1000 p

3.3.3 Silicon strip tracker

3.3.4 calorimeters

3.3.5 Superconducting solenoid magnet

The superconducting magnet installed is the CMS detector is designed to provide an intense and highly uniform magnetic field in the central part of the detector. In fact the tracking system take advantage of the bending power of the magnetic field to measure with precision the momentum of the particles that traverse it. The magnet has a diameter of 6.3 m, a lenght of 12.5 m in a cold mass of 220 t; the generated a magnetic fiels reach a strength of 3.8T. Since it is made of Ni-Tb superconducting cable it has to operate at a temperature of 4.7 K by using a heluim cryogenic system; the current circulating in the cables reach 18800 A under normal running conditions.

The left side of figure 3.11 shows an artistic view of the CMS magnet, while the right side shows a transverse view of the cold mass where the winding structure is visible.

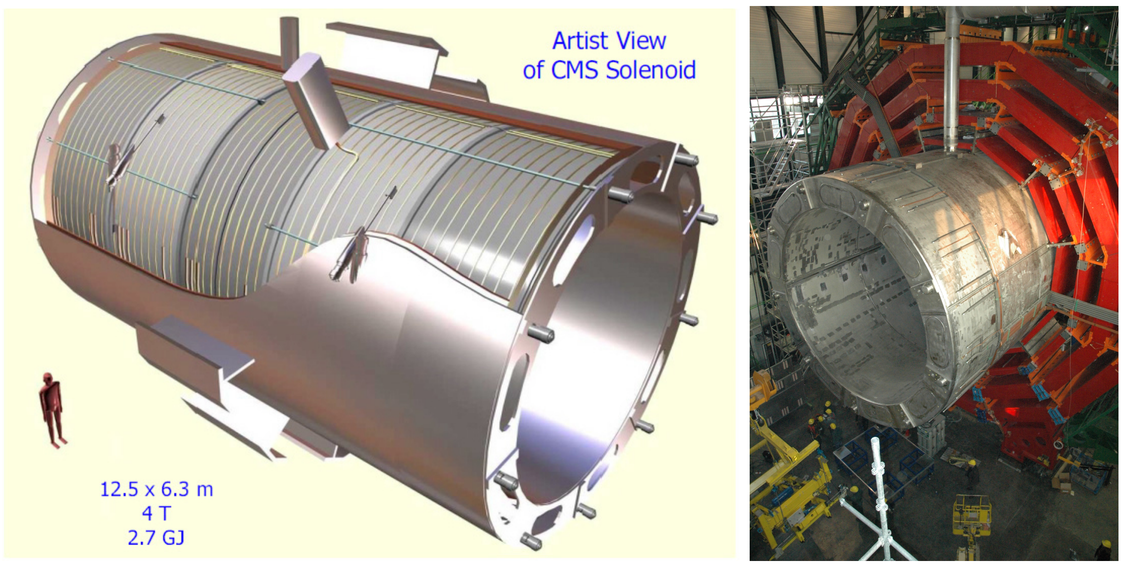

Figure 3.11: Artistic representation of the CMS solenoid magnet(left). The magnet is supported on an iron yoke (right) which also serves as the house of the muon detector and as mechanical support for the whole CMS detector [74].

The yoke (see figure 3.11), composed of 5 barrel wheels and 6 endcap disks made of iron, serves not only as the media for magnetic flux return, but also provides the house for the muon detector sytem and structural stability to the full detector.

3.3.6 muon system

3.3.7 trigger system - HLT- L1

. The online event selection process (trigger) must reduce the huge rate to about 100 events/s for storage and subsequent analysis. The short time between bunch crossings, 25 ns, has major implications for the design of the read-out and trigger systems.

3.3.8 computing model

3.4 Event generation simulation and reconstruction

3.4.1 event generation

3.4.2 Hard scattering

3.4.3 parton shower

3.4.4 hadronization and decays

3.4.5 underlying events and pileup

3.4.6 MC - MadEvent, MadGraph and madgraphNLO, powheg, pythia, tauola

3.4.7 detector simulation

3.4.8 event reconstruction- particle flow algorithm, vertexing , muon reco, electron reco, photon and hadron reco, jets reco, anti-kt algoritm, jet energy corrections, btagging, MET

3.4.9 MVA methods, NN, BDT, boosting, overtraining, variable ranking

3.4.10 statistical inference, likelihood parametrization

3.4.11 nuisance paraeters

Chapter 4

Search for production of a Higgs boson and a single top quark in multilepton final states in pp collisions at $\sqrt{s} = 13$ TeV

4.1 Introduction

Dont forget to mention previous constrains to ct check reference **??** and references

https://link.springer.com/content/pdf/10.1007%2FJHEP01

A. Azatov, R. Contino and J. Galloway, âĂIJModel-Independent Bounds on a Light Higgs,âĂİ JHEP 1204 (2012) 127 [arXiv:1202.3415 [hep-ph]].

J. R. Espinosa, C. Grojean, M. Muhlleitner and M. Trott, âĂIJFingerprinting Higgs Suspects at the LHC,âĂİ JHEP 1205 (2012) 097 [arXiv:1202.3697 [hep-ph]].

This chapter present the search for the associated production of a Higgs boson and a single top quark events with three leptons in the final state, targeting Higgs decay modes to WW, ZZ, and $\tau\tau$. The analysis uses the 13 TeV dataset produced in 2016, corresponding to an integrated luminosity of $35.9fb^{-1}$. It is based on and expands previous analyses at 8 TeV [75, 76] and searches for associated production of $t\bar{t}$ and Higgs in the same channel [77], and complements searches in other decay channels targeting $H \to b\bar{b}$ [78].

As showed in section 2.4, the cross section of the associated production of a Higgs boson and a single top quark (tHq) process is driven by a destructive interference of two contributions (see Figure 4.1), where the Higgs couples to either the W boson or the top quark. Any deviation from the standard model (SM) in the Higgs coupling structure could therefore lead to a large enhancement of the cross section, making this analysis sensitive to such deviations. A second process, where the Higgs and top quark are accompanied by a W boson (tHW) has similar behavior, albeit with a weaker interference pattern.

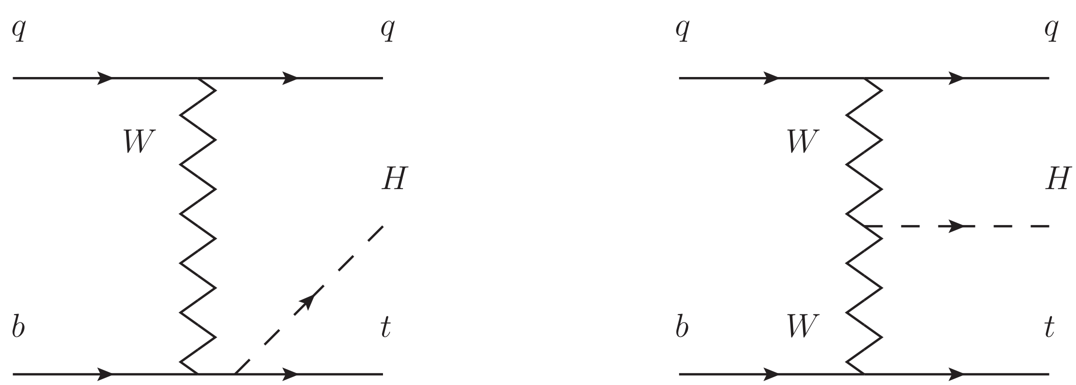

Figure 4.1: The two leading-order diagrams of tHq production.

We selects events with three leptons and a b tagged jet in the final state. The tHq signal contribution is then determined in a fit of the observed data to two multivariate classifier outputs, each trained to discriminate against one of the two dominant backgrounds of events with non-prompt leptons from $t\bar{t}$ and of associated production of $t\bar{t}$

and vector bosons ($t\bar{t}W$, $t\bar{t}Z$). The fit result is then used to set an upper limit on the combined $t\bar{t}H$, tHq and tHWproduction cross section, as a function of the relative coupling strengths of Higgs and top quark and Higgs and W boson, respectively.

4.2 Data and MC Samples

The data considered in this analysis were collected by the CMS experiment during 2016 and correspond to a total integrated luminosity of $35.9 fb^{-1}$. Only periods when the CMS magnet was on were considered when selecting the data samples, that corresponds to the 23 Sep 2016 (Run B to G) and PromptReco (Run H) versions of the datasets. The MC samples used in this analysis correspond to the RunIISummer16MiniAODv2 campaign produced with CMSSW 80X. The two signal samples (for tHq and tHW) were produced with MG5_aMC@NLO (version 5.222), in leading-order order mode, and are normalized to next-to-leading-order cross sections, see Tab. 4.1.Each sample is generated with a set of event weights corresponding to different values of κ_t and κ_{V} couplings as shown in Tab. 4.2.

4.2.1 Full 2016 dataset and MC samples

Sample	σ [pb]	BF
`/THQ_Hincl_13TeV-madgraph-pythia8_TuneCUETP8M1/`	0.7927	0.324
`/THW_Hincl_13TeV-madgraph-pythia8_TuneCUETP8M1/`	0.1472	1.0

Table 4.1: Signal samples and their cross section and branching fraction used in this analysis. See Ref. [79] for more details.

Different MC generators were used to generate the background processes. The dominant sources ($t\bar{t}$, $t\bar{t}W$, $t\bar{t}Z$, $t\bar{t}H$) were produced using aMC@NLO interfaced to PYTHIA8, and are scaled to NLO cross sections. Other processes are simulated

		tHq		tHW		
κ_{V}	κ_t	sum of weights	cross section [pb]	sum of weights	cross section [pb]	LHE weights
1.0	-3.0	35.700022	2.991	11.030445	0.6409	LHEweight_wgt[446]
1.0	-2.0	20.124298	1.706	5.967205	0.3458	LHEweight_wgt[447]
1.0	-1.5	14.043198	1.205	4.029093	0.2353	LHEweight_wgt[448]
1.0	-1.25	11.429338	0.9869	3.208415	0.1876	LHEweight_wgt[449]
1.0	-1.0		0.7927		0.1472	
1.0	-0.75	7.054998	0.6212	1.863811	0.1102	LHEweight_wgt[450]
1.0	-0.5	5.294518	0.4723	1.339886	0.07979	LHEweight_wgt[451]
1.0	-0.25	3.818499	0.3505	0.914880	0.05518	LHEweight_wgt[452]
1.0	0.0	2.627360	0.2482	0.588902	0.03881	LHEweight_wgt[453]
1.0	0.25	1.719841	0.1694	0.361621	0.02226	LHEweight_wgt[454]
1.0	0.5	1.097202	0.1133	0.233368	0.01444	LHEweight_wgt[455]
1.0	0.75	0.759024	0.08059	0.204034	0.01222	LHEweight_wgt[456]
1.0	1.0	0.705305	0.07096	0.273617	0.01561	LHEweight_wgt[457]
1.0	1.25	0.936047	0.0839	0.442119	0.02481	LHEweight_wgt[458]
1.0	1.5	1.451249	0.1199	0.709538	0.03935	LHEweight_wgt[459]
1.0	2.0	3.335034	0.2602	1.541132	0.08605	LHEweight_wgt[460]
1.0	3.0	10.516125	0.8210	4.391335	0.2465	LHEweight_wgt[461]
1.5	-3.0	45.281492	3.845	13.426212	0.7825	LHEweight_wgt[462]
1.5	-2.0	27.606715	2.371	7.809713	0.4574	LHEweight_wgt[463]
1.5	-1.5	20.476088	1.784	5.594971	0.3290	LHEweight_wgt[464]
1.5	-1.25	17.337465	1.518	4.635978	0.2749	LHEweight_wgt[465]
1.5	-1.0	14.483302	1.287	3.775902	0.2244	LHEweight_wgt[466]
1.5	-0.75	11.913599	1.067	3.014744	0.1799	LHEweight_wgt[467]
1.5	-0.5	9.628357	0.874	2.352505	0.1410	LHEweight_wgt[468]
1.5	-0.25	7.627574	0.702	1.789184	0.1081	LHEweight_wgt[469]
1.5	0.0	5.911882	0.5577	1.324946	0.08056	LHEweight_wgt[470]
1.5	0.25	4.479390	0.4365	0.959295	0.05893	LHEweight_wgt[471]
1.5	0.5	3.331988	0.3343	0.692727	0.04277	LHEweight_wgt[472]
1.5	0.75	2.469046	0.2558	0.525078	0.03263	LHEweight_wgt[473]
1.5	1.0	1.890565	0.2003	0.456347	0.02768	LHEweight_wgt[474]
1.5	1.25	1.596544	0.1689	0.486534	0.02864	LHEweight_wgt[475]
1.5	1.5	1.586983	0.1594	0.615638	0.03509	LHEweight_wgt[476]
1.5	2.0	2.421241	0.2105	1.170602	0.06515	LHEweight_wgt[477]
1.5	3.0	7.503280	0.5889	3.467546	0.1930	LHEweight_wgt[478]
0.5	-3.0	27.432685	2.260	8.929074	0.5136	LHEweight_wgt[479]
0.5	-2.0	13.956013	1.160	4.419093	0.2547	LHEweight_wgt[480]
0.5	-1.5	8.924438	0.7478	2.757611	0.1591	LHEweight_wgt[481]
0.5	-1.25	6.835341	0.5726	2.075247	0.1204	LHEweight_wgt[482]
0.5	-1.0	5.030704	0.4273	1.491801	0.08696	LHEweight_wgt[483]
0.5	-0.75	3.510528	0.2999	1.007273	0.05885	LHEweight_wgt[484]
0.5	-0.5	2.274811	0.1982	0.621663	0.03658	LHEweight_wgt[485]
0.5	-0.25	1.323555	0.1189	0.334972	0.01996	LHEweight_wgt[486]
0.5	0.0	0.656969	0.06223	0.147253	0.008986	LHEweight_wgt[487]
0.5	0.25	0.274423	0.02830	0.058342	0.003608	LHEweight_wgt[488]
0.5	0.5	0.176548	0.01778	0.068404	0.003902	LHEweight_wgt[489]
0.5	0.75	0.363132	0.03008	0.177385	0.009854	LHEweight_wgt[490]
0.5	1.0	0.834177	0.06550	0.385283	0.02145	LHEweight_wgt[491]
0.5	1.25	1.589682	0.1241	0.692099	0.03848	LHEweight_wgt[492]
0.5	1.5	2.629647	0.2047	1.097834	0.06136	LHEweight_wgt[493]
0.5	2.0	5.562958	0.4358	2.206057	0.1246	LHEweight_wgt[494]
0.5	3.0	14.843102	1.177	5.609519	0.3172	LHEweight_wgt[495]

Table 4.2: κ_{V} and κ_t combinations generated for the two signal samples and their NLO cross sections. The tHq cross section is multiplied by the branching fraction of the enforced leptonic decay of the top quark (0.324). See also Ref. [79].

Sample	σ [pb]
`TTWJetsToLNu_TuneCUETP8M1_13TeV-amcatnloFXFX-madspin-pythia8`	0.2043
`TTZToLLNuNu_M-10_TuneCUETP8M1_13TeV-amcatnlo-pythia8`	0.2529
`ttHJetToNonbb_M125_13TeV_amcatnloFXFX_madspin_pythia8_mWCutfix`	0.2151
`/store/cmst3/group/susy/gpetrucc/13TeV/u/TTLL_m1to10_LO_NoMS_for76X/`	0.0283
`WGToLNuG_TuneCUETP8M1_13TeV-madgraphMLM-pythia8`	585.8
`ZGTo2LG_TuneCUETP8M1_13TeV-amcatnloFXFX-pythia8`	131.3
`TGJets_TuneCUETP8M1_13TeV_amcatnlo_madspin_pythia8`	2.967
`TGJets_TuneCUETP8M1_13TeV_amcatnlo_madspin_pythia8`	2.967
`TTGJets_TuneCUETP8M1_13TeV-amcatnloFXFX-madspin-pythia8`	3.697
`WpWpJJ_EWK-QCD_TuneCUETP8M1_13TeV-madgraph-pythia8`	0.03711
`ZZZ_TuneCUETP8M1_13TeV-amcatnlo-pythia8`	0.01398
`WWZ_TuneCUETP8M1_13TeV-amcatnlo-pythia8`	0.1651
`WZZ_TuneCUETP8M1_13TeV-amcatnlo-pythia8`	0.05565
`WW_DoubleScattering_13TeV-pythia8`	1.64
`tZq_ll_4f_13TeV-amcatnlo-pythia8_TuneCUETP8M1`	0.0758
`ST_tWll_5f_LO_13TeV-MadGraph-pythia8`	0.01123
`TTTT_TuneCUETP8M1_13TeV-amcatnlo-pythia8`	0.009103
`WZTo3LNu_TuneCUETP8M1_13TeV-powheg-pythia8`	4.4296
`ZZTo4L_13TeV_powheg_pythia8`	1.256
`TTJets_SingleLeptFromTbar_TuneCUETP8M1_13TeV-madgraphMLM-pythia8`	182.1754
`TTJets_SingleLeptFromT_TuneCUETP8M1_13TeV-madgraphMLM-pythia8`	182.1754
`TTJets_DiLept_TuneCUETP8M1_13TeV-madgraphMLM-pythia8`	87.3
`DYJetsToLL_M-10to50_TuneCUETP8M1_13TeV-amcatnloFXFX-pythia8`	18610
`DYJetsToLL_M-50_TuneCUETP8M1_13TeV-madgraphMLM-pythia8`	6024
`WJetsToLNu_TuneCUETP8M1_13TeV-amcatnloFXFX-pythia8`	61526.7
`ST_tW_top_5f_inclusiveDecays_13TeV-powheg-pythia8_TuneCUETP8M1`	35.6
`ST_tW_antitop_5f_inclusiveDecays_13TeV-powheg-pythia8_TuneCUETP8M1`	35.6
`ST_t-channel_4f_leptonDecays_13TeV-amcatnlo-pythia8_TuneCUETP8M1`	70.3144
`ST_t-channel_antitop_4f_leptonDecays_13TeV-powheg-pythia8_TuneCUETP8M1`	26.2278
`ST_s-channel_4f_leptonDecays_13TeV-amcatnlo-pythia8_TuneCUETP8M1`	3.68064
`WWTo2L2Nu_13TeV-powheg`	10.481

Table 4.3: List of background samples used in this analysis (CMSSW 80X). In the first section of the table are listed the samples of the processes for which we use the simulation to extract the final yields and shapes, in the second section the samples of the processes we will estimate from data. The MC simulation is used to design the data driven methods and derive the associated systematics.

Sample	σ [pb]
`ttWJets_13TeV_madgraphMLM`	0.6105
`ttZJets_13TeV_madgraphMLM`	0.5297/0.692

Table 4.4: Leading-order $t\bar{t}W$ and $t\bar{t}Z$ samples used in the signal BDT training.

using POWHEG interfaced to PYTHIA, or bare PYTHIA (see table 4.3 and [77] for more details).

Three lepton and Four lepton
HLT_DiMu9_Ele9_CaloIdL_TrackIdL_v*
HLT_Mu8_DiEle12_CaloIdL_TrackIdL_v*
HLT_TripleMu_12_10_5_v*
HLT_Ele16_Ele12_Ele8_CaloIdL_TrackIdL_v*
HLT_Mu23_TrkIsoVVL_Ele8_CaloIdL_TrackIdL_IsoVL_v*
HLT_Mu23_TrkIsoVVL_Ele8_CaloIdL_TrackIdL_IsoVL_DZ_v*
HLT_Mu8_TrkIsoVVL_Ele23_CaloIdL_TrackIdL_IsoVL_v*
HLT_Mu8_TrkIsoVVL_Ele23_CaloIdL_TrackIdL_IsoVL_DZ_v*
HLT_Ele23_Ele12_CaloIdL_TrackIdL_IsoVL_DZ_v*
HLT_Mu17_TrkIsoVVL_Mu8_TrkIsoVVL_DZ_v*
HLT_Mu17_TrkIsoVVL_TkMu8_TrkIsoVVL_DZ_v*
HLT_IsoMu22_v*
HLT_IsoTkMu22_v*
HLT_IsoMu22_eta2p1_v*
HLT_IsoTkMu22_eta2p1_v*
HLT_IsoMu24_v*
HLT_IsoTkMu24_v*
HLT_Ele27_WPTight_Gsf_v*
HLT_Ele25_eta2p1_WPTight_Gsf_v*
HLT_Ele27_eta2p1_WPLoose_Gsf_v*

Table 4.5: Table of high-level triggers that we consider in the analysis.

4.2.2 Triggers

We consider online-reconstructed events triggered by one, two, or three leptons. Single-lepton triggers are included to boost the acceptance of events where the p_T of the sub-leading lepton falls below the threshold of the double-lepton triggers. Additionally, by including double-lepton triggers in the $\geq$ 3 lepton category, as well as single-lepton triggers in all categories, we increase the efficiency, considering the logical "or" of the trigger decisions of all the individual triggers in a given category. Tab. 4.5 shows the lowest-threshold non-prescaled triggers present in the High-Level Trigger (HLT) menus for both Monte-Carlo and data in 2016.

4.2.2.1 Trigger efficiency scale factors

The efficiency of events to pass the trigger is measured in simulation (trivially using generator information) and in the data (using event collected by an uncorrelated

Category	Scale Factor
ee	1.01 ± 0.02
eμ	1.01 ± 0.01
$\mu\mu$	1.00 ± 0.01
3l	1.00 ± 0.03

Table 4.6: Trigger efficiency scale factors and associated uncertainties, shown here rounded to the nearest percent.

MET trigger). Small differences between the data and MC efficiencies are corrected by applying scale factors as shown in Tab. 4.6. The exact procedure and control plots are documented in [80] for the current analysis.

4.3 Object Identification and event selection

4.3.1 Jets and b tagging

The analysis uses anti-k_t (0.4) particle-flow (PF) jets, corrected for charged hadrons not coming from the primary vertex (charged hadron subtraction), and having jet energy corrections (`Summer16_23Sep2016V3`) applied as a function of the jet E_T and η. Jets are only considered if they have a transverse energy above 25GeV.

In addition, they are required to be separated from any lepton candidates passing the fakeable object selections (see Tables 4.7 and 4.8) by $\Delta\mathrm{R} > 0.4$.

The loose and medium working points of the CSV b-tagging algorithm are used to identify b jets. Data/simulation differences in the b tagging performance are corrected by applying per-jet weights to the simulation, dependent on the jet p_T, eta, b tagging discriminator, and flavor (from simulation truth) [81]. The per-event weight is taken as the product of the per-jet weights, including those of the jets associated to the leptons. More details can be found in the corresponding $t\bar{t}H$ documentation [77, 80].

4.3.2 Lepton selection

Cut	Loose	Fakeable object	Tight
$\lvert\eta\rvert < 2.4$	✓	✓	✓
p_T	$> 5GeV$	$> 15GeV$	$> 15GeV$
$\lvert d_{xy}\rvert < 0.05$ (cm)	✓	✓	✓
$\lvert d_z\rvert < 0.1$ (cm)	✓	✓	✓
$\mathrm{SIP}_{3D} < 8$	✓	✓	✓
$I_{\mathrm{mini}} < 0.4$	✓	✓	✓
is Loose Muon	✓	✓	✓
jet CSV	–	< 0.8484	< 0.8484
is Medium Muon	–	–	✓
tight-charge	–	–	✓
lepMVA > 0.90	–	–	✓

Table 4.7: Requirements on each of the three muon selections. In the cases where the cut values change between the selections, those values are listed in the table. Otherwise, whether the cut is applied is indicated. For the two p_T^{ratio} and CSV rows, the cuts marked with a † are applied to leptons that fail the lepton MVA cut, while the loose cut value is applied to those that pass the lepton MVA cut.

The lepton reconstruction and selection is identical to that used in the $t\bar{t}H$ multilepton analysis, as documented in Refs. [77, 80]. For details on the reconstruction algorithms, isolation, pileup mitigation, and a description of the lepton MVA discriminator and validation plots thereof, we refer to that document since they are out of the scope of this thesis. Three different selections are defined both for the electron and muon object identification: the *Loose*, *Fakeable Object*, and *Tight* selection. As described in more detail later, these are used for event level vetoes, the fake rate estimation application region, and the final signal selection, respectively. The p_T of fakeable objects is defined as $0.85 \times p_T(\mathrm{jet})$, where the jet is the one associated to the lepton object. This mitigates the dependence of the fake rate on the momentum of the fakeable object and thereby improves the precision of the method.

Tables 4.7 and 4.8 list the full criteria for the different selections of muons and electrons.

Cut	Loose	Fakeable Object	Tight
$\lvert\eta\rvert < 2.5$	✓	✓	✓
p_T	$> 7GeV$	$> 15GeV$	$> 15GeV$
$\lvert d_{xy}\rvert < 0.05$ (cm)	✓	✓	✓
$\lvert d_z\rvert < 0.1$ (cm)	✓	✓	✓
$\mathrm{SIP}_{3D} < 8$	✓	✓	✓
$I_{\mathrm{mini}} < 0.4$	✓	✓	✓
MVA ID $> (0.0, 0.0, 0.7)$	✓	✓	✓
$\sigma_{i\eta i\eta} < (0.011, 0.011, 0.030)$	–	✓	✓
H/E $< (0.10, 0.10, 0.07)$	–	✓	✓
$\Delta\eta_{in} < (0.01, 0.01, 0.008)$	–	✓	✓
$\Delta\phi_{in} < (0.04, 0.04, 0.07)$	–	✓	✓
$-0.05 < 1/E - 1/p < (0.010, 0.010, 0.005)$	–	✓	✓
p_T^{ratio}	–	$> 0.5\dagger$ / –	–
jet CSV	–	$< 0.3\dagger$ / < 0.8484	< 0.8484
tight-charge	–	–	✓
conversion rejection	–	–	✓
Number of missing hits	< 2	$== 0$	$== 0$
lepMVA > 0.90	–	–	✓

Table 4.8: Criteria for each of the three electron selections. In cases where the cut values change between selections, those values are listed in the table. Otherwise, whether the cut is applied is indicated. In some cases, the cut values change for different η ranges. These ranges are $0 < \lvert\eta\rvert < 0.8$, $0.8 < \lvert\eta\rvert < 1.479$, and $1.479 < \lvert\eta\rvert < 2.5$ and the respective cut values are given in the form (value$_1$, value$_2$, value$_3$).

4.3.3 Lepton selection efficiency

Efficiencies of reconstruction and selecting loose leptons are measured both for muons and electrons using a tag and probe method on both data and MC, using $Z \to \ell^+\ell^-$. Corresponding scale factors are derived from the ratio of efficiencies and applied to the selected These. Events are produced for the leptonic SUSY analyses using equivalent lepton selections and recycled for the $t\bar{t}H$ analysis as well as for this analysis. The efficiencies of applying the tight selection as defined in Tables 4.7 and 4.8, on the loose leptons are determined again by using a tag and probe method on a sample of DY-enriched events. They are documented for the $t\bar{t}H$ analysis in Ref. [80] and are exactly equivalent for this analysis.

4.4 Background predictions

The modeling of reducible and irreducible backgrounds in this analysis uses the exact methods, analysis code, and ROOT trees used for the $t\bar{t}H$ multilepton analysis. We give a brief description of the methods and refer to the documentation of that analysis in Refs. [77, 80] for any details.

The backgrounds in three-lepton final states can be split in two broad categories: irreducible backgrounds with genuine prompt leptons (i.e. from on-shell W and Z boson decays); and reducible backgrounds where at least one of the leptons is "non-prompt", i.e. produced within a hadronic jet, either a genuine lepton from heavy flavor decays, or simply mis-reconstructed jets.

Irreducible backgrounds can be reliantly estimated directly from Monte-Carlo simulated events, using higher-order cross sections or data control regions for the overall normalization. This is done in this analysis for all backgrounds involving prompt leptons: $t\bar{t}W$, $t\bar{t}Z$, $t\bar{t}H$, WZ, ZZ, $W^{\pm}W^{\pm}qq$, $t\bar{t}t\bar{t}$, tZq, tZW, WWW, WWZ, WZZ, ZZZ.

Reducible backgrounds, on the other hand, are not well predicted by simulation, and are estimated using data-driven methods. In the case of non-prompt leptons, a fake rate method is used, where the contribution to the final selection is estimated by extrapolating from a sideband (or "application region") with a looser lepton definition (the fakeable object definitions in Tabs. 4.7 and 4.8) to the signal selection. The tight-to-loose ratios (or "fake rates") are measured in several background dominated data events with dedicated triggers, subtracting the residual prompt lepton contribution using MC. Non-prompt leptons in our signal regions are predominantly produced in $t\bar{t}$ events, with a much smaller contribution, from Drell–Yan production. The systematic uncertainty on the normalization of the non-prompt background estimation is on the order of 50%, and thereby one of the dominant limitations on the performance of multilepton analyses in general and this analysis in particular. It consists of several individual sources, such as the result of closure tests of the method using simulated events, limited statistics in the data control regions due to necessary prescaling of lepton triggers, and the uncertainty in the subtraction of residual prompt leptons from the control region.

The fake background where the leptons pass the looser selection are weighted according to how many of them fail the tight criteria. Events with a single failing lepton are weighted with the factor $f/(1-f)$ for the estimate to the tight selection region, where f is the fake rate. Events with two failing leptons are given the negative weight $-f_i f_j/(1-f_i)(1-f_j)$, and for three leptons the weight is positive and equal to the product of $f/(1-f)$ factor evaluated for each failing lepton.

Figures 4.2 show the distributions of some relevant kinematic variables, normalized to the cross section of the respective processes and to the integrated luminosity.

4.5 Signal discrimination

The tHq signal is separated from the main backgrounds using a boosted decision tree (BDT) classifier, trained on simulated signal and background events. A set of discriminating variables are given as input to the BDT which produces a output distribution maximizing the discrimination power. Table 4.9 lists the input variables used while Figures 4.3 show their distributions for the relevant signal and background samples, for the three lepton channel. Two BDT classifiers are trained for the two main backgrounds expected in the analysis: events with prompt leptons from $t\bar{t}W$and $t\bar{t}Z$(also referred to as $t\bar{t}$V), and events with non-prompt leptons from $t\bar{t}$. The datasets used in the training are the tHq signal (see Tab. 4.1), and LO MADGRAPH samples

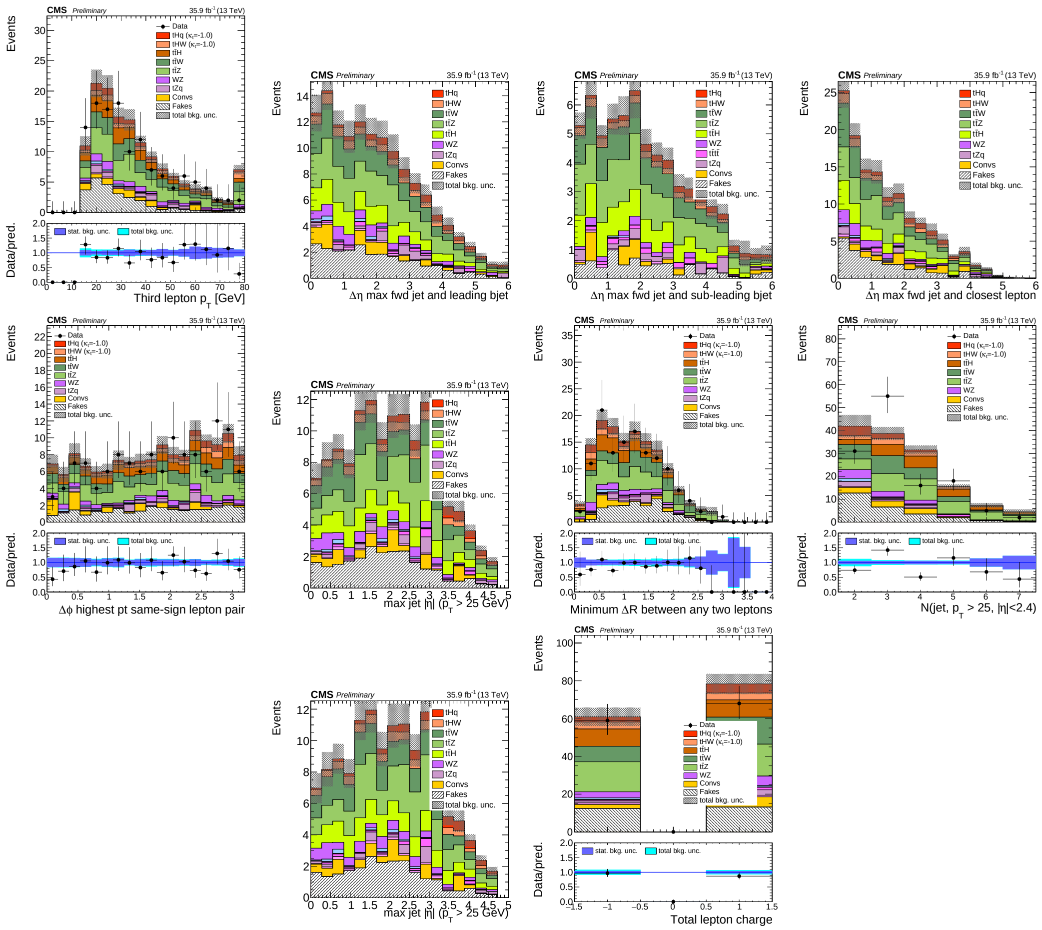

Figure 4.2: Distributions of input variables to the BDT for signal discrimination, three lepton channel, normalized to their cross section and to $35.9 fb^{-1}$.

of $t\bar{t}W$ and $t\bar{t}Z$, in an admixture proportional to their respective cross sections (see Tab. 4.4).

The MVA analysis consist of two stages: first a “training” where the MVA method is trained to discriminate between simulated signal and background events, then a “test” stage where the trained algorithm is used to classify different events from the samples. The sample is obtained from a pre-selection (see Tab. **??** with pre-selection cuts). Figures 4.4 show the input variables distributions as seen by the MVA algorithm. Note that in contrast to the distributions in Fig. 4.3 only the main backgrounds ($t\bar{t}$ from simulation, $t\bar{t}$V) are included.

Variable name	Description
nJet25	Number of jets with $p_T > 25$ GeV, $\|\eta\| < 2.4$
MaxEtaJet25	Maximum $\|\eta\|$ of any (non-CSV-loose) jet with $p_T > 25$ GeV
totCharge	Sum of lepton charges
nJetEta1	Number of jets with $\|\eta\| > 1.0$, non-CSV-loose
detaFwdJetBJet	$\Delta\eta$ between forward light jet and hardest CSV loose jet
detaFwdJet2BJet	$\Delta\eta$ between forward light jet and second hardest CSV loose jet (defaults to -1 in events with only one CSV loose jet)
detaFwdJetClosestLep	$\Delta\eta$ between forward light jet and closest lepton
dphiHighestPtSSPair	$\Delta\phi$ of highest p_T same-sign lepton pair
minDRll	minimum ΔR between any two leptons
Lep3Pt/Lep2Pt	p_T of the 3^{rd} lepton (2^{nd} for ss2l)

Table 4.9: MVA input discriminating variables

Note that splitting the training in two groups reveals that some variables show opposite behavior for the two background sources; potentially screening the discrimination power if they were to be used in a single discriminant. For some other variables the distributions are similar in both background cases.

From table 4.9, it is clear that the input variables are correlated to some extend. These correlations play an important role for some MVA methods like the Fisher discriminant method in which the first step consist of performing a linear transformation to an phase space where the correlations between variables are removed. In case a boosted decision tree (BDT) method however, correlations do not affect the performance. Figure 4.6 show the linear correlation coefficients for signal and background for the two training cases (the signal values are identical by construction). As expected, strong correlations appears for variables related to the forward jet activity. Same trend is seen in case of the same sign dilepton channel in Figure **??**.

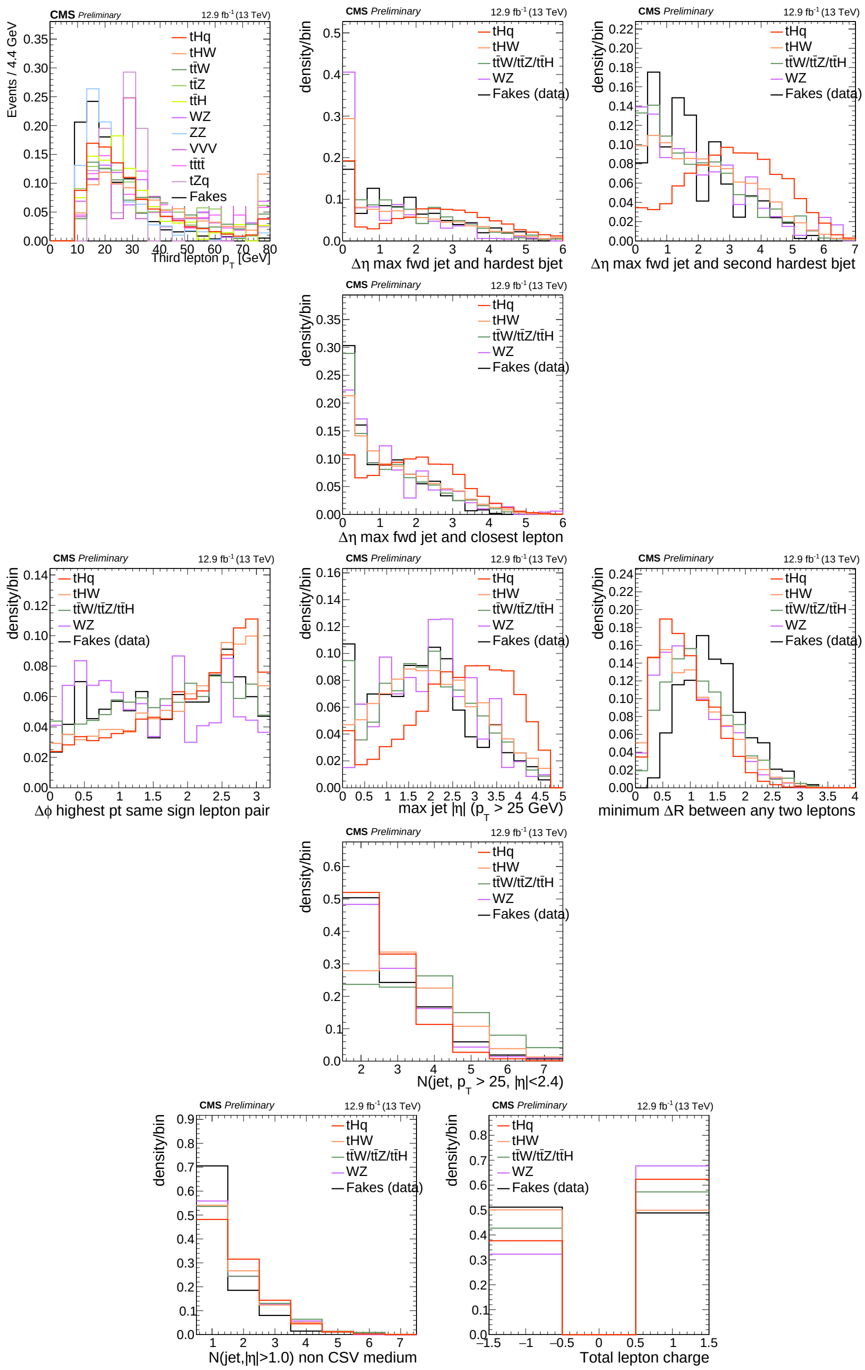

Figure 4.3: Distributions of input variables to the BDT for signal discrimination, three lepton channel.

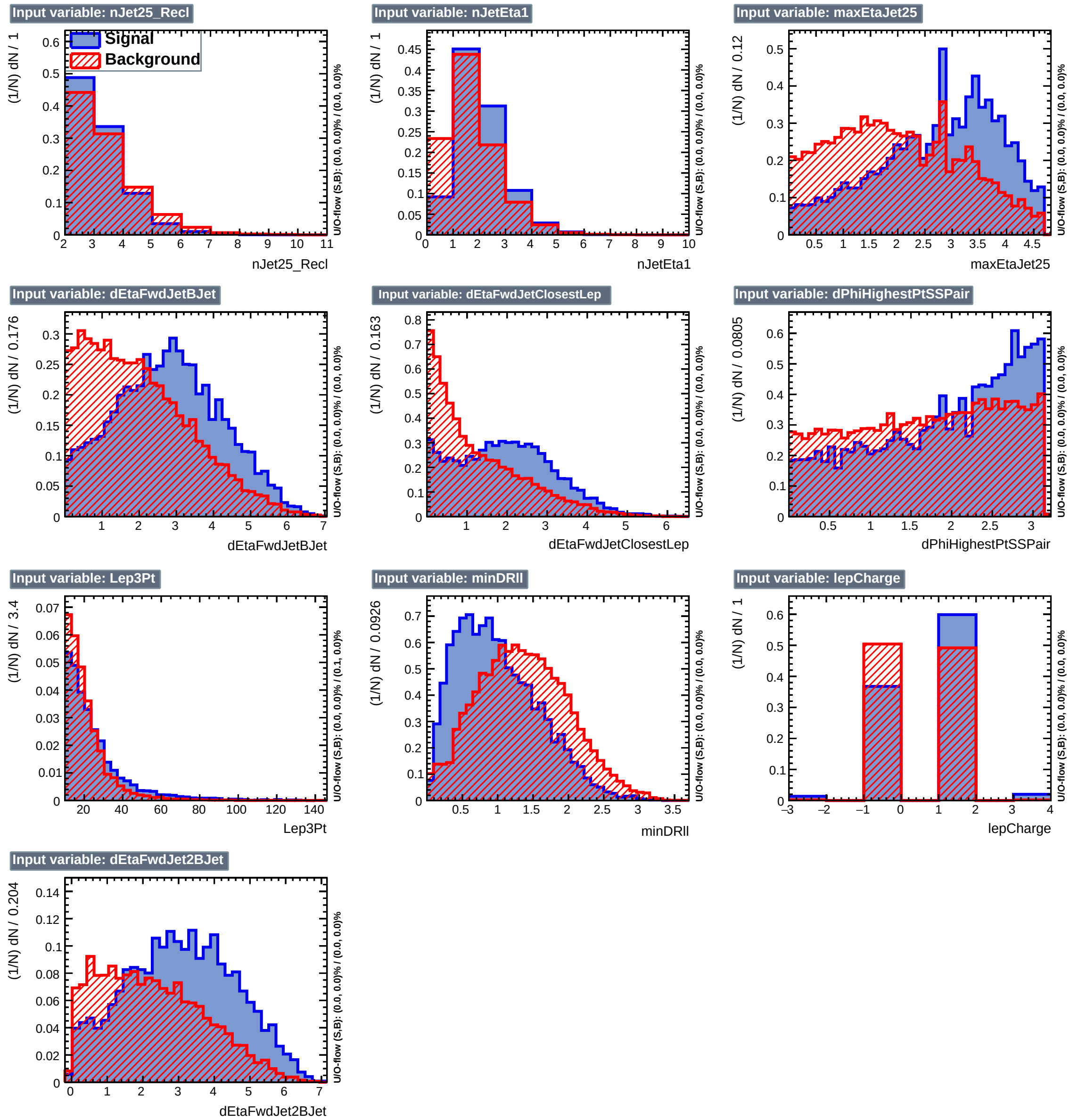

Figure 4.4: BDT inputs as seen by TMVA (signal, in blue, is tHq, background, in red, is $t\bar{t}$) for the three lepton channel, discriminated against $t\bar{t}$ (fakes) background.

4.5.1 Classifiers response

Several MVA algorithms were evaluated to determine the most appropriate method for this analysis. The plots in Fig. 4.7 (top) show the background rejection as a function of the signal efficiency for $t\bar{t}$ and $t\bar{t}$V trainings (ROC curves) for the different

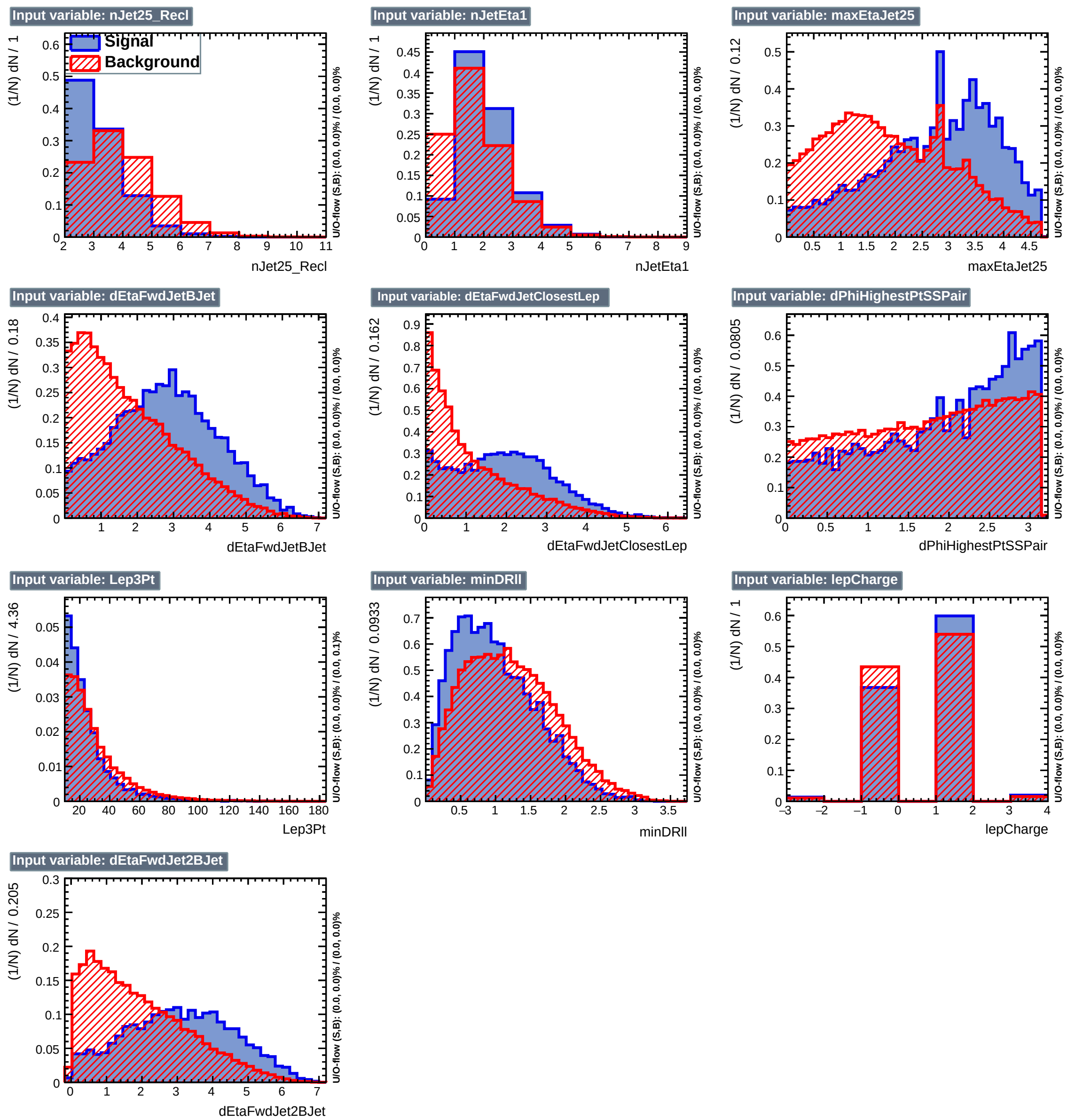

Figure 4.5: BDT inputs as seen by TMVA (signal, in blue, is tHq, background, in red, is $t\bar{t}W+t\bar{t}Z$) for the three lepton channel, discriminated against $t\bar{t}$V background.

algorithms that were evaluated.

In both cases the gradient boosted decision tree ("BDTA_GRAD") classifier offers the best results, followed by an adaptive BDT classifier ("BDTA"). The BDTA_GRAD classifier output distributions for signal and backgrounds are shown on the bottom of Fig. 4.7. As expected, a good discrimination power is obtained using default discrim-

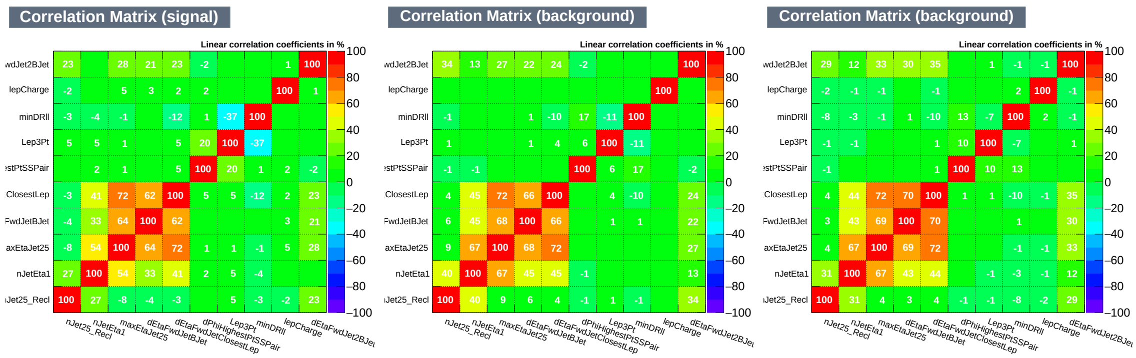

Figure 4.6: Signal (left), $t\bar{t}$ background (middle), and $t\bar{t}$V background (right.) correlation matrices for the input variables in the TMVA analysis for the three lepton channel.

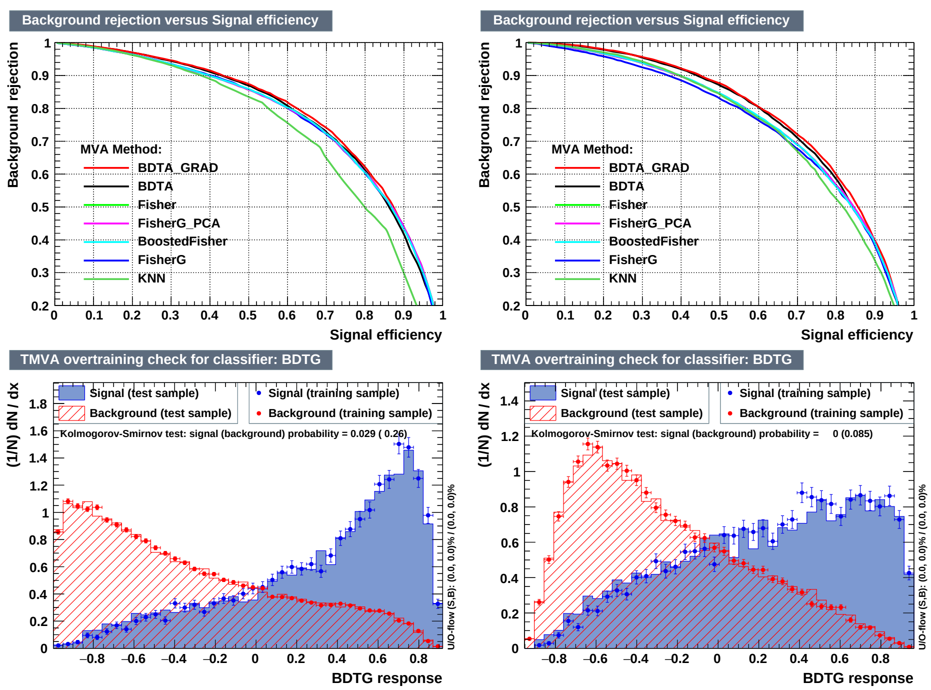

Figure 4.7: Top: background rejection vs signal efficiency (ROC curves) for various MVA classifiers (top) in the three lepton channel against $t\bar{t}$V (left) and $t\bar{t}$ (right). Bottom: classifier output distributions for the gradient boosted decision trees, for training against $t\bar{t}$V (left) and against $t\bar{t}$ (right).

inator parameter values, with minimal overtraining. TMVA provides a ranking of the input variables by their importance in the classification process, shown in Tab. 4.10.

The TMVA settings used in the BDT training are shown in Tab. 4.11.

	ttbar training		ttV training	
Rank	Variable	Importance	Variable	Importance
1	minDRll	1.329e-01	dEtaFwdJetBJet	1.264e-01
2	dEtaFwdJetClosestLep	1.294e-01	Lep3Pt	1.224e-01
3	dEtaFwdJetBJet	1.209e-01	maxEtaJet25	1.221e-01
4	dPhiHighestPtSSPair	1.192e-01	dEtaFwdJet2BJet	1.204e-01
5	Lep3Pt	1.158e-01	dEtaFwdJetClosestLep	1.177e-01
6	maxEtaJet25	1.121e-01	minDRll	1.143e-01
7	dEtaFwdJet2BJet	9.363e-02	dPhiHighestPtSSPair	9.777e-02
8	nJetEta1	6.730e-02	nJet25_Recl	9.034e-02
9	nJet25_Recl	6.178e-02	nJetEta1	4.749e-02
10	lepCharge	4.701e-02	lepCharge	4.116e-02

Table 4.10: TMVA input variables ranking for BDTA_GRAD method for the trainings in the three lepton channel. For both trainings the rankings show almost the same 5 variables in the first places.

```
TMVA.Types.kBDT
NTrees=800
BoostType=Grad
Shrinkage=0.10
!UseBaggedGrad
nCuts=50
MaxDepth=3
NegWeightTreatment=PairNegWeightsGlobal
CreateMVAPdfs
```

Table 4.11: TMVA configuration used in the BDT training.

4.6 Additional discriminating variables

Two additional discriminating variables were tested considering the fact that the forward jet in the background could come from the pileup; since we have a real forward jet in the signal, it could give some improvement in the discriminating power. The additional variables describe the forward jet momentum (fwdJetPt25) and the forward jet identification(fwdJetPUID). Distributions for these variables in the three lepton channel are shown in the figure 4.8. The forward jet identification distribution show that for both, signal and background, jets are mostly real jets.

The testing was made including in the MVA input one variable at a time, so we

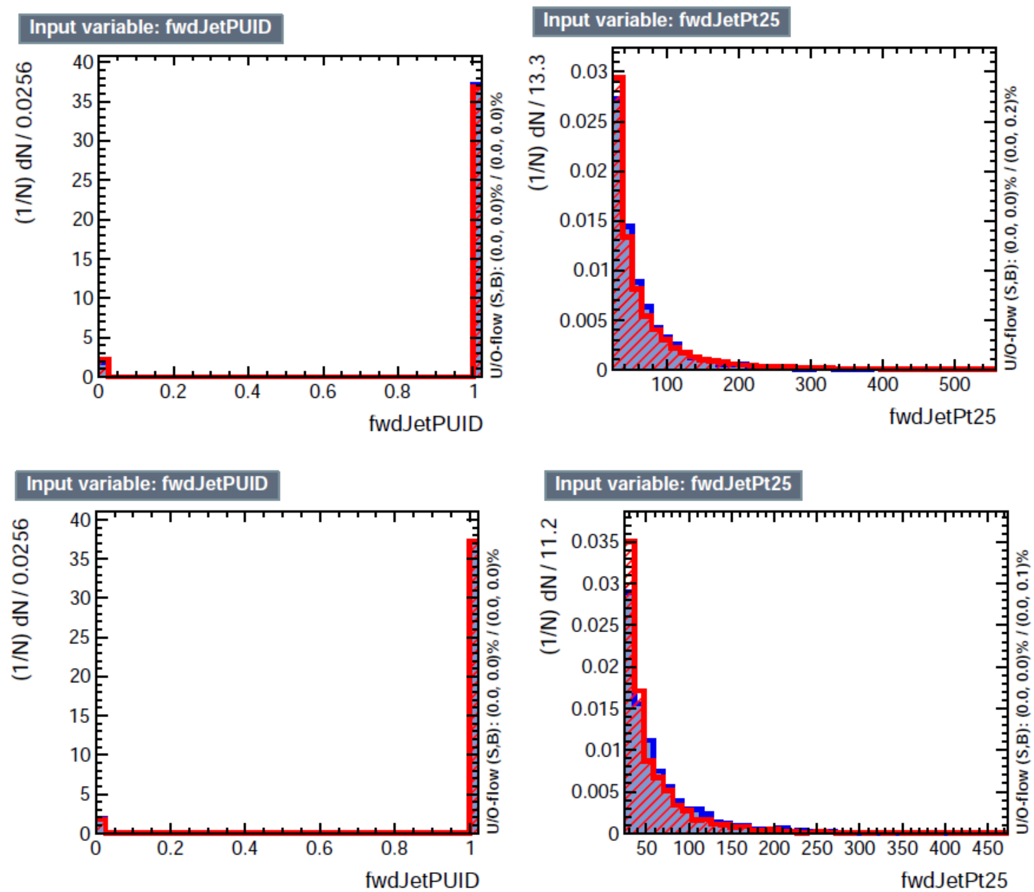

Figure 4.8: Additional discriminating variables distributions for ttv training(Top row) and tt training (bottom row) in the three lepton channel. The origin of the jets in the forward jet identification distribution is tagged as 0 for "pileup jets" while "real jets" are tagged as 1.

can evaluate the dicrimination power of each variable, and then both simultaneously. fwdJetPUID was ranked in the last place in importance (11) in both training (ttV and tt) while fwdJetPt25 was ranked 3 in the ttV training and 7 in the tt training. When training using 12 variables, fwdJetPt25 was ranked 5 and 7 in the ttV and tt trainings respectively, while fwdJetPUID was ranked 12 in both cases.

The improvement in the discrimination performance provided by the additional variables is about 1%, so it was decided not to include them in the procedure. Table 4.12 show the ROC-integral for all the testing cases we made.

	ROC-integral
base 10 var ttv	0.848
+ fwdJetPUID ttv	0.849
+ fwdJetPt25 ttv	0.856
12 var ttv	0.856
base 10 var tt	0.777
+ fwdJetPUID tt	0.777
+ fwdJetPt25 tt	0.787
12 var	0.787

Table 4.12: ROC-integral for all the testing cases we made in the evaluation of the additional variables discriminating power. The improvement in the discrimination performance provided by the additional variables is about 1%

Chapter 5

The CMS forward pixel detector

5.0.1 The phase 1 FPix upgrade

5.0.2 FPix module production line

5.0.3 The Gluing stage

5.0.4 The Encapsulation stage

5.0.5 The FPix module production yields

References

[1] D.J. Griffiths, “Introduction to electrodynamics”. 4th ed. Pearson, (2013).

[2] F. Mandl, G. Shaw. “Quantum field theory.” Chichester: Wiley (2009).

[3] F. Halzen, and A.D. Martin, “Quarks and leptons: An introductory course in modern particle physics”. New York: Wiley, (1984) .

[4] J.C. Maxwell. “A dynamical theory of the electromagnetic field”. Philosophical Transactions of the Royal Society of London. 155: 459âĂŞ512.(1865) doi:10.1098/rstl.1865.0008

[5] M. Planck. “ÃIJber das Gesetz der Energieverteilung im Normalspektrum”. Annalen der Physik. 4 (3): 553.(1901).

[6] A. Einstein “ÃIJber einen die Erzeugung und Verwandlung des Lichtes betreffenden heuristischen Gesichtspunkt”. Annalen der Physik. 17 (6): 132âĂŞ148, (1905).

[7] A. Einstein. “ÃIJber die von der molekularkinetischen Theorie der WÃďrme geforderte Bewegung von in ruhenden FlÃijssigkeiten suspendierten Teilchen”. Annalen der Physik. 17 (8): 549âĂŞ560, (1905).

[8] A. Einstein. “Zur Elektrodynamik bewegter KÃűrper”. Annalen der Physik. 17 (10): 891âĂŞ921, (1905).

[9] A. Einstein, “Ist die TrÃďgheit eines KÃűrpers von seinem Energieinhalt abhÃďngig?”. Annalen der Physik. 18 (13): 639âĂŞ641, (1905).

[10] B. P. Abbott et al. “Observation of Gravitational Waves from a Binary Black Hole Merger”. PRL 116, 061102 (2016).

[11] J. Schwinger. “Quantum Electrodynamics. I. A Covariant Formulation”. Physical Review. 74 (10): 1439âĂŞ61, (1948).

[12] R. P. Feynman. “SpaceâĂŞTime Approach to Quantum Electrodynamics”. Physical Review. 76 (6): 769âĂŞ89, (1949).

[13] S. Tomonaga. “On a Relativistically Invariant Formulation of the Quantum Theory of Wave Fields”. Progress of Theoretical Physics. 1 (2): 27âĂŞ42, (1946).

[14] S.L. Glashow. “Partial symmetries of weak interactions”, Nucl. Phys. 22 579-588, (1961).

[15] A. Salam, J.C. Ward. “Electromagnetic and weak interactions”, Physics Letters 13 168-171, (1964).

[16] S. Weinberg, “A model of leptons”, Physical Review Letters, vol. 19, no. 21, p. 1264, (1967).

[17] E. Noether, “Invariante Variationsprobleme”, Nachrichten von der Gesellschaft der Wissenschaften zu GÃűttingen, mathematisch-physikalische Klasse, vol. 1918, pp. 235âĂŞ257, (1918).

[18] File:Standard_Model_of_Elementary_Particle_dark.svg. (2017, June 12) Wikimedia Commons, the free media repository. Retrieved November 27, 2017 from $https://www.collegiate-advanced-electricity.com/single-post/2017/04/10/The-Standard-Model-of-Particle-Physics$.

[19] M. Goldhaber, L. Grodzins, A.W. Sunyar “Helicity of Neutrinos”, Phys. Rev. 109, 1015 (1958).

[20] Palanque-Delabrouille N et al. “Neutrino masses and cosmology with Lyman-alpha forest power spectrum”,JCAP 11 011 (2015).

[21] C. Patrignani et al. (Particle Data Group), Chin. Phys. C, 40, 100001 (2016) and 2017 update.

[22] M. Gell-Mann. “A Schematic Model of Baryons and Mesons”. Physics Letters. 8 (3): 214âĂŞ215 (1964).

[23] G. Zweig. “An SU(3) Model for Strong Interaction Symmetry and its Breaking” (PDF). CERN Report No.8182/TH.401 (1964).

[24] G. Zweig. “An SU(3) Model for Strong Interaction Symmetry and its Breaking: II” (PDF). CERN Report No.8419/TH.412(1964).

[25] M. Gell-Mann. “The Interpretation of the New Particles as Displaced Charged Multiplets”. Il Nuovo Cimento 4: 848. (1956).

[26] T. Nakano, K, Nishijima. “Charge Independence for V-particles”. Progress of Theoretical Physics 10 (5): 581-582. (1953).

[27] N. Cabibbo, “Unitary symmetry and leptonic decays” Physical Review Letters, vol. 10, no. 12, p. 531, (1963).

[28] M.Kobayashi, T.Maskawa, “CP-violation in the renormalizable theory of weak interaction,” Progress of Theoretical Physics, vol. 49, no. 2, pp. 652-657, (1973).

[29] File:Weak Decay (flipped).svg. (2017, June 12). Wikimedia Commons, the free media repository. Retrieved November 27, 2017

from $https : //commons.wikimedia.org/w/index.php?title = File : Weak\_Decay\_(flipped).svg\&oldid = 247498592$.

[30] Georgia Tech University. Coupling Constants for the Fundamental Forces(2005). Retrieved January 10, 2018, from $http : //hyperphysics.phy - astr.gsu.edu/hbase/Forces/couple.html\#c2$

[31] M. Strassler. (May 31, 2013).The Strengths of the Known Forces. Retrieved January 10, 2018, from $https : //profmattstrassler.com/articles - and - posts/particle - physics - basics/the - known - forces - of - nature/the - strength - of - the - known - forces/$

[32] M. Peskin, D. Schroeder, "An introduction to quantum field theory". Perseus Books Publishing L.L.C., (1995).

[33] A. Pich. "The Standard Model of Electroweak Interactions" https://arxiv.org/abs/1201.0537

[34] F.Bellaiche. (2012, 2 September). "What's this Higgs boson anyway?". Retrieved from: https://www.quantum-bits.org/?p=233

[35] M. Endres et al. Nature 487, 454-458 (2012) doi:10.1038/nature11255

[36] F. Englert, R. Brout. "Broken Symmetry and the Mass of Gauge Vector Mesons". Physical Review Letters. 13 (9): 321âĂŞ23.(1964) Bibcode:1964PhRvL..13..321E. doi:10.1103/PhysRevLett.13.321

[37] P.Higgs. "Broken Symmetries and the Masses of Gauge Bosons". Physical Review Letters. 13 (16): 508âĂŞ509,(1964). Bibcode:1964PhRvL..13..508H. doi:10.1103/PhysRevLett.13.508.

[38] G.Guralnik, C.R. Hagen and T.W.B. Kibble. “Global Conservation Laws and Massless Particles”. Physical Review Letters. 13 (20): 585âĂŞ587, (1964). Bibcode:1964PhRvL..13..585G. doi:10.1103/PhysRevLett.13.585.

[39] CMS collaboration. “Observation of a new boson at a mass of 125 GeV with the CMS experiment at the LHC”. Physics Letters B. 716 (1): 30âĂŞ61 (2012). arXiv:1207.7235. Bibcode:2012PhLB..716...30C. doi:10.1016/j.physletb.2012.08.021

[40] ATLAS collaboration. “Observation of a New Particle in the Search for the Standard Model Higgs Boson with the ATLAS Detector at the LHC”. Physics Letters B. 716 (1): 1âĂŞ29(2012). arXiv:1207.7214 Bibcode:2012PhLB..716....1A. doi:10.1016/j.physletb.2012.08.020.

[41] ATLAS collaboration; CMS collaboration (26 March 2015). “Combined Measurement of the Higgs Boson Mass in pp Collisions at âĹŽs=7 and 8 TeV with the ATLAS and CMS Experiments”. Physical Review Letters. 114 (19): 191803. arXiv:1503.07589. Bibcode:2015PhRvL.114s1803A. doi:10.1103/PhysRevLett.114.191803.

[42] CMS Collaboration, “SM Higgs Branching Ratios and Total Decay Widths (up-date in CERN Report4 2016)”. https://twiki.cern.ch/twiki/bin/view/LHCPhysics/CERNYellowReportPageBR , last accessed on 17.12.2017.

[43] R.Grant V. “Determination of Higgs branching ratios in $H \to W^+W^{\text{â}}$ĹŠ $\to l$Î $\cdot\, jj$ and $H \to ZZ \to l^+l^-jj$ channels”. Physics Department, University of Tennessee (Dated: October 31, 2012). Retrieved from http://aesop.phys.utk.edu/ph611/2012/projects/Riley.pdf

[44] LHC Higgs Cross Section Working Group, Denner, A., Heinemeyer, S. et al. “Standard model Higgs-boson branching ratios with uncertainties”. Eur. Phys. J. C (2011) 71: 1753. https://doi.org/10.1140/epjc/s10052-011-1753-8

[45] LHC InternationalMasterclasses“When protons collide”. Retrieved from http://atlas.physicsmasterclasses.org/en/zpath_protoncollisions.htm

[46] F. Maltoni, K. Paul, T. Stelzer, and S. Willenbrock, “Associated production of Higgs and single top at hadron colliders”, Phys.Rev. D64 (2001) 094023, [hep-ph/0106293].

[47] S. Biswas, E. Gabrielli, F. Margaroli, and B. Mele, “Direct constraints on the top-Higgs coupling from the 8 TeV LHC data,” Journal of High Energy Physics, vol. 07, p. 073, (2013).

[48] M. Farina, C. Grojean, F. Maltoni, E. Salvioni, and A. Thamm, “Lifting degeneracies in Higgs couplings using single top production in association with a Higgs boson,” Journal of High Energy Physics, vol. 05, p. 022, (2013).

[49] T.M. Tait and C.-P. Yuan, “Single top quark production as a window to physics beyond the standard model”, Phys. Rev. D 63 (2000) 014018 [hep-ph/0007298].

[50] F. Demartin, F. Maltoni, K. Mawatari, and M. Zaro, “Higgs production in association with a single top quark at the LHC,” European Physical Journal C, vol. 75, p. 267, (2015).

[51] CMS Collaboration, “Modelling of the single top-quark production in association with the Higgs boson at 13 TeV.” https://twiki.cern.ch/twiki/bin/viewauth/CMS/SingleTopHiggsGeneration13TeV, last accessed on 16.01.2018.

[52] CMS Collaboration, “SM Higgs production cross sections at $\sqrt{s} = 13$ TeV.” https://twiki.cern.ch/twiki/bin/view/LHCPhysics/CERNYellowReportPageAt13TeV, last accessed on 16.01.2018.

[53] S. Dawson, The effective W approximation, Nucl. Phys. B 249 (1985) 42.

[54] S. Biswas, E. Gabrielli and B. Mele, JHEP 1301 (2013) 088 [arXiv:1211.0499 [hep-ph]].

[55] F. Demartin, B. Maier, F. Maltoni, K. Mawatari, and M. Zaro, “tWH associated production at the LHC”, European Physical Journal C, vol. 77, p. 34, (2017). arXiv:1607.05862

[56] LHC Higgs Cross Section Working Group, “Handbook of LHC Higgs Cross Sections: 4.Deciphering the Nature of the Higgs Sector”, arXiv:1610.07922.

[57] J. Ellis, D. S. Hwang, K. Sakurai, and M. Takeuchi.“Disentangling Higgs-Top Couplings in Associated Production”, JHEP 1404 (2014) 004, [arXiv:1312.5736].

[58] CMS Collaboration, V. Khachatryan et al., “Precise determination of the mass of the Higgs boson and tests of compatibility of its couplings with the standard model predictions using proton collisions at 7 and 8 TeV,” arXiv:1412.8662.

[59] ATLAS and CMS Collaborations, “Measurements of the Higgs boson production and decay rates and constraints on its couplings from a combined ATLAS and CMS analysis of the LHC pp collision data at $sqrts = 7$ and 8 TeV,” (2016). CERN-EP-2016-100, ATLAS-HIGG-2015-07, CMS-HIG-15-002.

[60] File:Cern-accelerator-complex.svg. Wikimedia Commons, the free media repository. Retrieved January, 2018 from https://commons.wikimedia.org/wiki/File:Cern-accelerator-complex.svg

[61] J.L. Caron , “Layout of the LEP tunnel including future LHC infrastructures.”, (Nov, 1993). A C Collection. Legacy of AC. Pictures from 1992 to 2002. Retrieved from https://cds.cern.ch/record/841542

[62] M. Vretenar, “The radio-frequency quadrupole”. CERN Yellow Report CERN-2013-001, pp.207-223 DOI:10.5170/CERN-2013-001.207. arXiv:1303.6762

[63] L.Evans. P. Bryant (editors). “LHC Machine”. JINST 3 S08001 (2008).

[64] CERN Photographic Service.“Radio-frequency quadrupole, RFQ-1”, March 1983, CERN-AC-8303511. Retrieved from https://cds.cern.ch/record/615852.

[65] CERN Photographic Service “Animation of CERN’s accelerator network”, 14 October 2013. DOI: 10.17181/cds.1610170 Retrieved from https://videos.cern.ch/record/1610170

[66] C.Sutton. “Particle accelerator”.Encyclopedia Britannica. July 17, 2013. Retrieved from https://www.britannica.com/technology/particle-accelerator.

[67] L.Guiraud. “Installation of LHC cavity in vacuum tank.”. July 27 2000. CERN-AC-0007016. Retrieved from https://cds.cern.ch/record/41567.

[68] J.L. Caron, “Magnetic field induced by the LHC dipole’s superconducting coils”. March 1998. AC Collection. Legacy of AC. Pictures from 1992 to 2002. LHC-PHO-1998-325. Retrieved from https://cds.cern.ch/record/841511

[69] AC Team. “Diagram of an LHC dipole magnet”. June 1999. CERN-DI-9906025 retrieved from https://cds.cern.ch/record/40524.

[70] CMS Collaboration “Public CMS Luminosity Information”. https://twiki.cern.ch/twiki/bin/view/CMSPublic/LumiPublicResults#2016_proton_proton last accessed 24.01.2018

[71] J.L Caron. “LHC Layout” AC Collection. Legacy of AC. Pictures from 1992 to 2002. September 1997, LHC-PHO-1997-060. Retrieved from https://cds.cern.ch/record/841573.

[72] CMS Collaboration. “The CMS experiment at the CERN LHC” JINST 3 S08004 (2008).

[73] CMS Collaboration. “CMS detector drawings 2012” CMS-PHO-GEN-2012-002. Retrieved from http://cds.cern.ch/record/1433717.

[74] R. Breedon. “View through the CMS detector during the cooldown of the solenoid on February 2006. CMS Collection”, February 2006, CMS-PHO-OREACH-2005-004, Retrieved from https://cds.cern.ch/record/930094.

[75] CMS Collaboration, “Search for the associated production of a Higgs boson with a single top quark in proton-proton collisions at $\sqrt{s} = 8$ TeV”, JHEP 06 (2016) 177,doi:10.1007/JHEP06(2016)177, arXiv:1509.08159.

[76] B. Stieger, C. Jorda Lope et al., “Search for Associated Production of a Single Top Quark and a Higgs Boson in Leptonic Channels”, CMS Analysis Note CMS AN-14-140, 2014.

[77] M. Peruzzi, C. Mueller, B. Stieger et al., “Search for ttH in multilepton final states at $\sqrt{s} = 13$ TeV”, CMS Analysis Note CMS AN-16-211, 2016.

[78] CMS Collaboration, “Search for H to bbar in association with a single top quark as a test of Higgs boson couplings at $\sqrt{s} = 13$ TeV”, CMS Physics Analysis Summary CMS-PAS-HIG-16-019, 2016.

[79] B. Maier, “SingleTopHiggProduction13TeV”, February, 2016. https://twiki.cern.ch/twiki/bin/viewauth/CMS/SingleTopHiggsGeneration13TeV.

[80] M. Peruzzi, F. Romeo, B. Stieger et al., "Search for ttH in multilepton final1 states at $\sqrt{s} = 13$ TeV", CMS Analysis Note CMS AN-17-029, 2017.

[81] B. WG, "BtagRecommendation80XReReco", February, 2017. https://twiki.cern.ch/twiki/bin/view/CMS/BtagRecommendation80XReReco.